# ATLAS NOTE

January 25, 2010

# Simulation of ATLAS Luminosity Monitoring with LUCID

M.Bruschi[a], D.Caforio[a,b], L.Fabbri[a,b], J.Groth-Jensen[e], V.Hedberg[e],
C.Sbarra[a,b], A.Sbrizzi[a,b], M.Shupe[c], S.Valentinetti[a,b], M.Villa[a,b],
Y.Yao[d]

[a]*I.N.F.N. Sezione di Bologna, Italy*
[b]*University of Bologna, Italy*
[c]*University of Arizona, Tucson, USA*
[d]*University of Alberta, Edmonton, Canada*
[e]*University of Lund, Lund, Sweden*

## Abstract

Monte Carlo simulations are used to characterize the response of
LUCID and its performance as a luminosity monitoring system. All
results are obtained with a light LUCID geometry made of 32 (instead
of 40) Cerenkov tubes read out by photo-multipliers.

The performance of LUCID is evaluated with 9159 single $pp$ in-
elastic collisions generated with PHOJET at $\sqrt{s} = 14$ TeV and passed
through a GEANT3-GCALOR simulation of the full ATLAS detector.

Different algorithms to extract the average number of $pp$ interac-
tions per event up to $L = 10^{34} \ cm^{-2}s^{-1}$ are presented.

# Contents

# 1   Introduction

A method for the absolute determination of luminosity ($\mathscr{L}$) is the measurement of the rate R of a theoretically well-understood process, which - after correcting for acceptance $A$, efficiency $\varepsilon$, and backgrounds $B$ - can be directly translated into a luminosity measurement:

$$\mathscr{L} = \frac{R-B}{A \cdot \varepsilon \cdot \sigma} \tag{1}$$

Here the cross section of the process ($\sigma$) should be calculable to the required precision from theory or from unrelated experiments. Unfortunately, at hadron colliders where the initial state consists of quarks and gluons, such theoretically well calculable processes are few. Moreover, the acceptance and efficiency convolutions are typically dependent on theory (via the necessary simulations of the acceptance and efficiency), as well as dependent on experimental factors, such as luminosity itself (which affects the selection efficiency for the process).

The ALFA detector in ATLAS will use the method mentioned above by measuring the elastic scattering process which can be predicted theoretically with high accuracy. However, this can only be done with special beam optics and at very low luminosity and so ALFA cannot provide luminosity during normal ATLAS running.

LUCID is a detector dedicated to measure luminosity during normal data taking. It consists of 20 Cerenkov tubes on each side of the interaction point, 16 of which are read-out directly by photo-multipliers and 4 which are read-out by optical quartz fibers connected to multi-anode photo-multipliers. LUCID will measure luminosity by sampling a fraction of the inelastic interactions in ATLAS. The basic idea is in this case that one can obtain the luminosity from the counting rate of all inelastic interactions ($R_{in}$) and the total inelastic cross section ($\sigma_{in}$) since

$$\mathscr{L} = \frac{R_{in}}{\sigma_{in}} \tag{2}$$

Any measurement with LUCID will have to take into account the efficiency ($\varepsilon_{in}$) and acceptance ($A_{in}$) of the detector to the inelastic interactions and so the expression above changes to

$$\mathscr{L} = \frac{R_{lucid}}{A_{in} \cdot \varepsilon_{in} \cdot \sigma_{in}} \tag{3}$$

The combined efficiency and acceptance can be measured by real data if an unbiased minimum bias trigger is available. In other case it can be estimated by using Monte Carlo simulations. The uncertainty in the cross section is, at least at the start of LHC, expected to be large and so a calibration of the method using only

simulations will not give a very precise result. In order to reduce the uncertainty in the luminosity determination, the LUCID detector will therefore measure the rate of inelastic interactions while ALFA is taking data and from the absolute luminosity determined by ALFA, LUCID will be calibrated so that a rate measured by LUCID corresponds to an absolute luminosity. With other words the product $A_{in} \cdot \varepsilon_{in} \cdot \sigma_{in}$ will be calculated from a combined run with ALFA and LUCID. In this way LUCID can be used to measure luminosity without any knowledge of the inelastic cross section or the acceptance and efficiency of LUCID. Alternative calibration methods to ALFA is to calculate luminosity from W and Z bosons and compare it to the integrated LUCID rate or by measuring the LUCID rate during beam separation scans, so-called van der Meer scans.

Since $R_{in} = \mu \cdot f_{BX}$, where $\mu$ is the average number of inelastic interactions per bunch crossing and $f_{BX}$ is the bunch crossing rate (which can be calculated as $f_{BX} =$ number of filled bunch crossings$/3564 \cdot 40$ MHz), the problem of the luminosity determination can be rephrased as one in which the true value of $\mu$ has to be obtained by doing a measurement of the average number of inelastic interactions per bunch crossing

$$\mathscr{L} = \frac{\mu_{lucid} \cdot f_{BX}}{A_{in} \cdot \varepsilon_{in} \cdot \sigma_{in}} = k_{lucid} \cdot \mu_{lucid} \qquad (4)$$

where $k_{lucid}$ is a calibration constant.

The calibration method with ALFA described above assumes that the rate measured by LUCID is directly proportional to the true rate of inelastic events over many orders of magnitude. Or to put it differently, that $\mu_{lucid}$ is equal to the true number of inelastic interactions even when there is on average $20 - 30$ interactions per bunch crossing. It is easy to see that this cannot always be the case. Assume as an example that one simply uses the rate of events with a signal in LUCID to estimate the rate of inelastic interactions. At some high value of $\mu$ there will be at least one signal in LUCID in every event and if the inelastic interaction rate is then increased the LUCID rate will not increase i.e. the LUCID event rate is in this case useless for the determination of the inelastic rate and hence the luminosity. Long before the method becomes completely useless there is a regime where $\mu_{lucid}$ is not proportional to $\mu_{true}$. This effect of the detector rate not increasing linearly with the inelastic rate is called saturation. If instead the number of Cerenkov tubes with a signal above threshold is used to determine $\mu$ (so-called hit counting) then this measurement will also become useless at some very high $\mu$ when there is a hit in every tube for every bunch crossing. This mu-value will, however, be much larger than the saturation value observed in event counting. One way to prevent these saturation problems is to count particles instead of events or hits. If all particles in the LUCID acceptance could be counted accurately and used to estimate the inelastic rate then there would in principle not be any saturation problems. This is, however, technically difficult to do and particle counting is not implemented in the LUCID

electronics. Even if this method was available, it would suffer from other problems which would spoil the simple relationship $\mathscr{L} = k_{lucid} \cdot \mu_{lucid} = k'_{lucid} \cdot R_{lucid}$. One of these problems has to do with the fact that machine background will perhaps make it necessary to only use events with a requirement of at least one particle in each LUCID detector. This will eliminate background but also introduce combinatorial effects that spoils the simple assumption that $\mu_{true} = k'_{lucid} \cdot R_{lucid}$. Another problem is caused by the fact that the LUCID pulse-height spectrum is more or less continuous instead of having only a well defined peak for particles from the interaction point. The reason for this is that secondary particles gives in many cases a pulse-height that is lower than the particles from the interaction point and these signals are therefore lower than the cut in the LUCID electronics that defines a particle. When the number of interactions per bunch crossing increases the probability also increases that two or more secondary particles will give a combined signal that is above the threshold value. Low signal particles are in this way said to migrate from the lower part of the pulse-height spectrum to higher values and this is called the migration effect.

So to summarize one can say that there are three basic rates that one can measure and that can then be used to estimate $\mu$:

- event counting i.e. one count the number of bunch crossings with or without a signal in LUCID;

- hit counting i.e. one counts the number of tubes with a signal above threshold in LUCID;

- particle counting i.e. by looking at the pulse-height distribution one can determine the number of particles in each tube and in LUCID in total.

In the present set-up of the detector electronics only the event and hit counting methods are used in LUCID. These methods suffers from three problems that spoils $\mu_{true} = k'_{lucid} \cdot R_{lucid}$:

- saturation when a large change in $\mu$ gives a small or no change in the measured detector rate;

- combinatorial effects caused by requirements of having signals in both detectors;

- migration problems when particles that give small signals add up at high $\mu$ to produce a signal above threshold.

The main purpose of this note is to determine how these three problems will affect the measurement of $\mu$ when different event rates and hit rates are used to estimate it. It will be shown that for all methods that have been studied the simple relationship $\mu_{true} = k'_{lucid} \cdot R_{lucid}$ do not hold for all values of mu. New expressions will therefore be developed where $\mu_{true}$ is expressed as more complex functions of $R_{lucid}$ i.e. $\mu_{true} = f(\mu_{lucid}) = F(R_{lucid})$. These functions can still be calibrated with

ALFA at low $\mu$ or by other methods at higher $\mu$ (as long as the $\mu$ value is known). This note describes how the functions $f$ and $F$ can be determined from simulated data. A more precise method to determine them is to record a sample of data with LUCID when $\mu \ll 1$. The QDC spectrum from these events, the so-called reference sample, can be combined so that pulse height plots can be obtained for any value of mu. The pulse-height plots can then be converted into hit distributions that can be used to examine the luminosity algorithms. In this way it will be possible to determine the functional dependence discussed above from real data and not only Monte Carlo simulations.

The note is divided in two parts. The first part illustrates the geometrical description of LUCID (Section 2) and the study of the detector response (Sections 3 and 4). In the second part (Sections 5), Monte Carlo simulations of the full ATLAS detector are used to study the performance of LUCID as a luminosity monitoring system. The average number of $pp$ interaction per event is extracted from the measurement samples in a wide range of luminosities with several methods and the results are compared with the expected values.

# 2   Detector description

LUCID consists of two detector modules located at a distance of about 17 m from the *pp* interaction point (IP). Each module is made of twenty aluminum tubes surrounding the beam pipe and pointing at the IP (Figure 1).
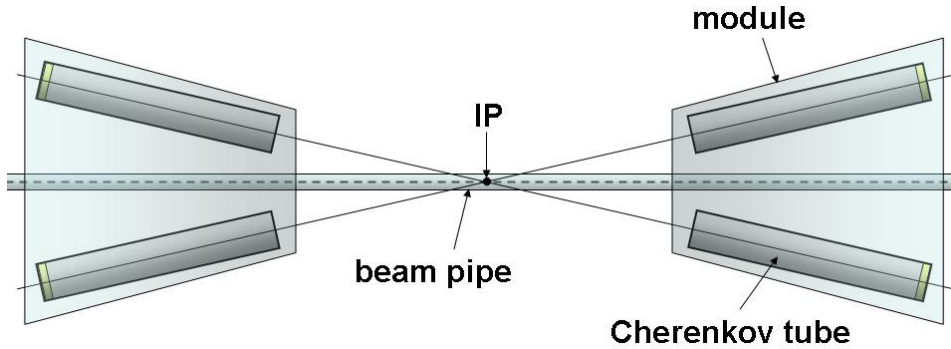


**Figure 1**. *Schematic view of the pointing geometry of four LUCID tubes (not in scale).*

Tubes are located in a pressure tight aluminum vessel which contains a Cerenkov gas radiator ($C_4F_{10}$ at 1.1 bar). Two rings of 8 tubes per module are directly coupled to photo-multipliers (Hamamatsu R762), while four tubes per module are read-out via optical fibers. A water based cooling system keeps the vessel temperature below the PMT critical value ($50°$ Celsius) during the beam-pipe bake-out operations.

A realistic simulation of the main LUCID detector elements (vessel, radiator, tubes, optical surfaces, PMTs and cooling system) has been developed in a standalone GEANT4 [1] simulation (version 4.7.1p01). A sketch of the geometrical description of a single Cerenkov tube is shown in Figure 2.
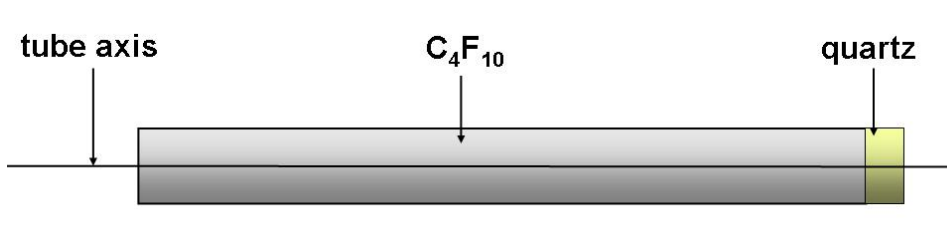


**Figure 2**. *Geometrical description of the Cerenkov tube (not in scale).*

The PMT is simulated with a thin quartz disc matching the transversal dimension of the tube. The photo-cathode and the chain of dynodes inside the PMT are not simulated. A photon crossing the surface of the window is detected with a probability corresponding to the quantum efficiency provided by Hamamatsu [2]. The simulation of the PMT quartz window is crucial since it acts as a photon emitter, in addition to the main gas radiator. All parameters used to describe the detector geometry are listed in Table 1.

| | |
|---|---|
| Distance from the IP [mm] | 16715.5 |
| Vessel length [mm] | 1532 |
| Vessel inner radius [mm] | 85 |
| Vessel outer radius [mm] | 125.15 (min), 147 (max) |
| Vessel inner thickness [mm] | 2.5 |
| Vessel outer thickness [mm] | 3.0 |
| Vessel bulkhead thickness [mm] | 3.2 |
| Cooling radius [mm] | 78 |
| Cooling thickness [mm] | 2 |
| Radial distance Tube-Beam [mm] | 96.3 (ring1) |
| Radial distance Tube-Beam [mm] | 114.7 (ring2) |
| Tube thickness [mm] | 1.0 |
| Tube length [mm] | 1495 |
| Tube radius [mm] | 7.0 |
| Pmt thickness [mm] | 1.2 |
| Pmt radius [mm] | 7.0 |
| Gas pressure [bar] | 1.1 |
| Gas temperature [kelvin] | 293.15 |

**Table 1**. *Parameters used for the geometrical description of LUCID.*

## 2.1 Cerenkov light emission

Cerenkov light is emitted when a charged particle traverses a material with a velocity $v$ larger than the speed of light in the medium $c/n$:

$$v > \frac{c}{n} \rightarrow \beta = \frac{v}{c} > \frac{1}{n} \tag{5}$$

where $n$ is the refractive index of the radiator. A basic description of Cerenkov light emission can be found in [3]. The minimal velocity at which the emission takes place is $c/n$ and corresponds to a particle energy threshold $E_{th}$ such that:

$$E_{th} = \gamma m_0 c^2 = \frac{m_0 c^2}{\sqrt{1 - \left(\frac{v}{c}\right)^2}} = \frac{m_0 c^2}{\sqrt{1 - \left(\frac{1}{n}\right)^2}} \tag{6}$$

where $m_0$ is the rest mass of the particle. For $\pi$ in $C_4F_{10}$ (quartz), $E_{th}$ is 2700 MeV (190 MeV). For $e$ in $C_4F_{10}$ (quartz), $E_{th}$ is 9.3 MeV (0.7 MeV).

## 2.1 Cerenkov light emission

The emission angle $\theta_C$ is a function of the refractive index of the medium and of the particle velocity:

$$\cos\theta_C = \frac{1}{\beta n}. \tag{7}$$

The refractive index of a gas is a function of the emitted photon energy ($E$), the pressure ($P$) and the temperature ($T$) of the gas [4]. In case of $C_4F_{10}$:

$$n = \sqrt{\frac{2x+1}{1-x}}, \quad \text{where} \quad x = \frac{0.25938 \times P[\text{bar}]}{T[\text{kelvin}]} \frac{1}{1 - \left(\frac{E[\text{eV}]}{17.0}\right)^2}. \tag{8}$$

The refractive index of quartz is calculated with the Sellmeier equation [5]:

$$n = 1 + \sqrt{\frac{46.41}{10.666^2 - E^2[\text{eV}]} + \frac{228.71}{18.125^2 - E^2[\text{eV}]} + \frac{0.014}{0.125^2 - E^2[\text{eV}]}}. \tag{9}$$

The refractive index of $C_4F_{10}$ and quartz are shown in Figure 3.
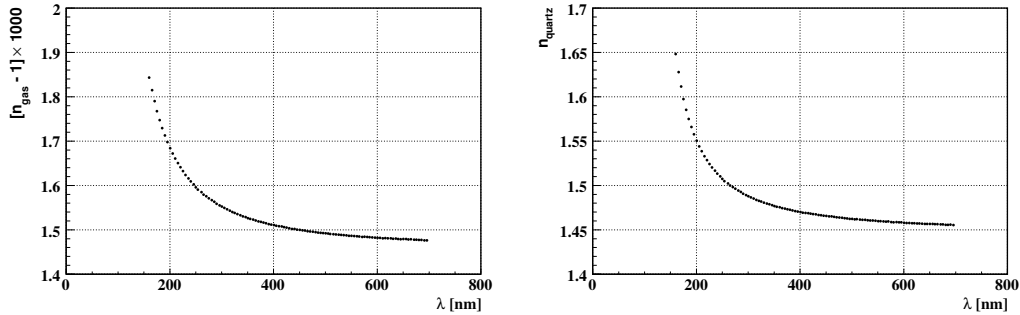


**Figure 3**. *Refractive index of $C_4F_{10}$ (left) and quartz (right) as a function of the wavelength.*

The average number of photons emitted per unit of radiator length ($L$) in the wavelength range $[\lambda_1, \lambda_2]$ is approximately given by the formula [6]:

$$\frac{dN}{dx[\text{nm}]} = 2\pi\alpha \int_{\lambda_2}^{\lambda_1} \sin^2\theta_C \frac{d\lambda}{\lambda^2} = 2\pi\alpha \int_{\lambda_2}^{\lambda_1} \left[1 - \left(\frac{1}{\beta n}\right)^2\right] \frac{d\lambda}{\lambda^2}. \tag{10}$$

Assuming a $C_4F_{10}$ (quartz) average refractive index of 1.00150 (1.47), which gives an average emission angle of 3.1° (46.8°), a relativistic particle crossing a tube along its axis ($\beta \approx 1$) at $P = 1.1$ bar and $T = 293.15°$ kelvin emits about 990 (140) photons in the gas (quartz) in the wavelength range [160, 700] nm. Therefore, density and thickness of the PMT window are such that Cerenkov photons from the window are not negligible compared to those from the gas.

## 2.2 Light propagation and detection

After being emitted in $C_4F_{10}$ with a typical angle of $3°$, photons are reflected by the inner walls of the tube with a certain efficiency (reflectivity). A typical aluminum surface reflectivity as a function of the photon wavelength can be found in [7]. This curve has been rescaled to match a bench measurement performed with red light. Depending on the position where they are generated, multiple reflections might occur before they actually reach the read-out photo-multipliers (Figure 4).
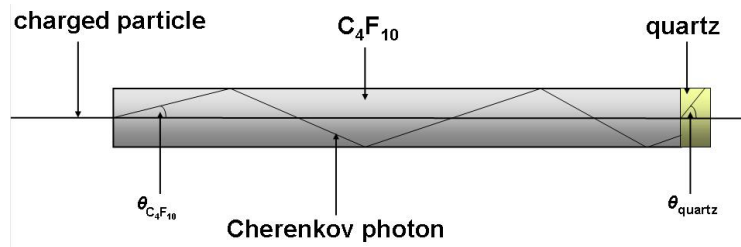
**Figure 4**. *Light propagation inside a tube.*

The average number of light reflections inside the tube is 2.8. Photons which are not absorbed by the gas reach the end of the tube and are converted by the PMTs into photo-electrons. The conversion efficiency (quantum efficiency) is wavelength dependent and is provided by the manufacturer (Hamamatsu) [2]. Tube reflectivity and quantum efficiency in the wavelength range accepted by the PMTs [160 nm, 700 nm] are shown in Figure 5 (numerical values are reported in Appendix A).
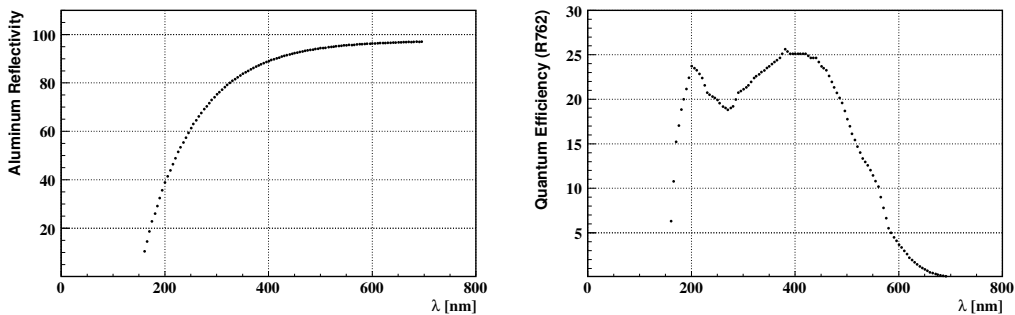
**Figure 5**. *Aluminum tube reflectivity (left) and PMT quantum efficiency (right) as a function of photon wavelength.*

Note that the dependence of reflectivity on photon polarization is not simulated. The absorption length of $C_4F_{10}$ is assumed to be similar to that of Isobutane [4] (numerical values are reported in Appendix A). The effect of absorption in the quartz is contained in the quantum efficiency.

# 3 Response to a single particle

LUCID geometry is such that a particle originating from the IP (a primary particle) produces more light than a particle coming from any other direction (a secondary particle). The response of LUCID is simulated for particles originating from the IP traveling either along the tube axis (on-axis) or a random direction (off-axis).

## 3.1 Signal from on-axis pions

A charged particle entering the tube and traveling along its axis emits Cerenkov photons in the gas and in the PMT quartz window. The number of photo-electrons read-out by the PMTs when 180 GeV charged pions travel along a tube axis is shown in Figure 6 (the signals in all 32 tubes are displayed).
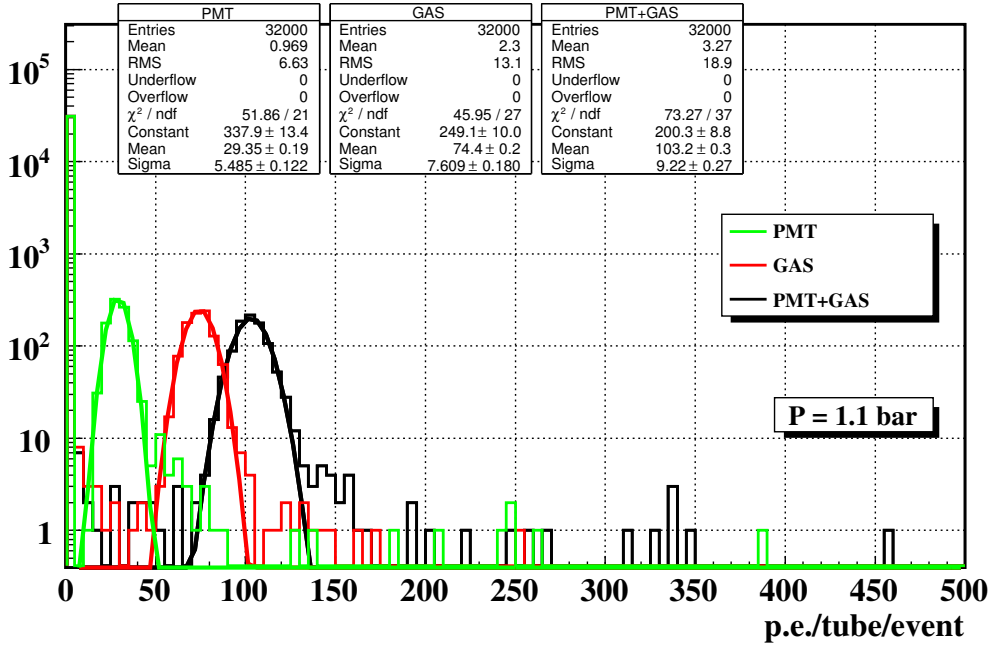


**Figure 6**. *Distribution of photo-electrons detected by LUCID in* 1000 *events of single charged pions coming from the IP with E = 180 GeV, $\theta = 0.00689$ and $\phi = 0$.*

The red (green) histogram in the left plot of Figure 6 represents Cerenkov light emitted in the gas (quartz) and detected by the PMT. A total signal of 105 photo-electrons (black histogram) is produced by a particle traveling along a tube axis (75 from the gas and 30 from the PMT). The peak at zero is due to the fact that only one tube per event is crossed by a particle. Solid lines are the results of Gaussian fits. The value of the width is due to two contributions: the Poissonian fluctuation of Cerenkov emission and the binomial fluctuation of photo-electron conversion inside the PMT.

10

The wavelength spectrum of Cerenkov light at different stages inside a LUCID tube is shown in the right plot of Figure 7.
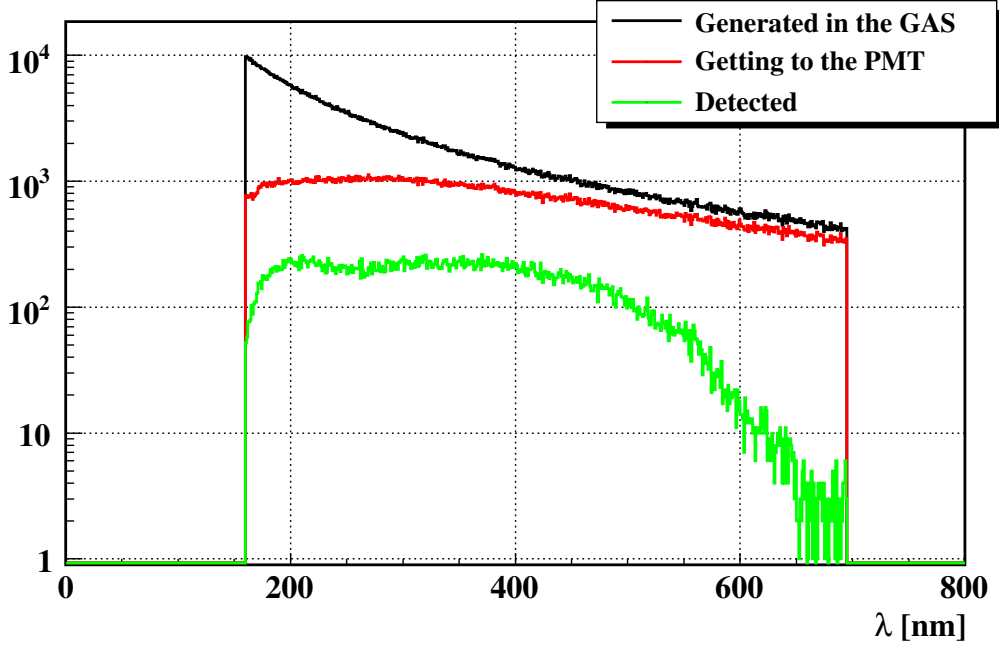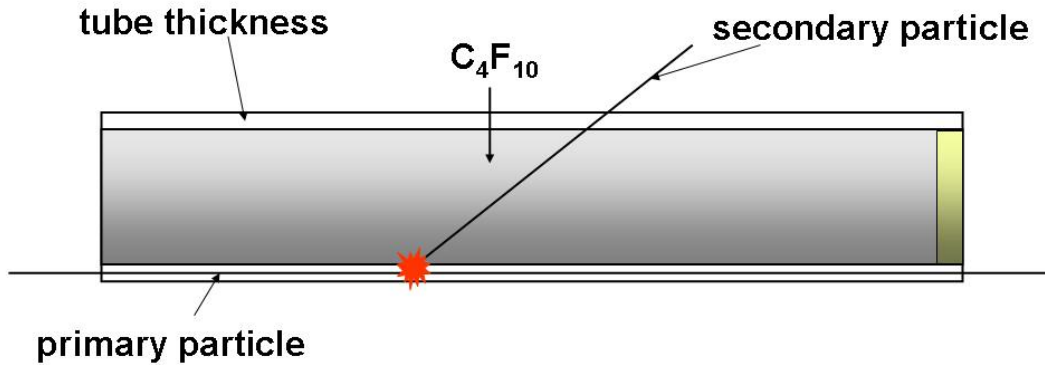


**Figure 7**. *Wavelength distribution of Cherenkov photons genereted in LUCID at in* 1000 *events of single charged pions coming from the IP with E* = 180 *GeV,* θ = 0.00689 *and* φ = 0. *The wavelength distribution of the fraction of photons reaching the PMT and finally detected are superimposed.*

The wavelength of generated photons (black line) has approximately a $1/\lambda^2$ shape. Generated photons traverse the gas and are reflected by the aluminum tube walls until they reach the quartz window (red line): the suppression at low $\lambda$ is due to the absorption inside the gas and to the aluminum reflectivity. The effect of quantum efficiency is visible in the spectrum of detected photons (green line), which is strongly suppressed above 600 nm.

## 3.2    Signal from off-axis pions

Particles originating from *pp* collisions typically travel along directions different from the tube axis. When a primary particle crosses the detector tube walls, secondary particles are produced by interaction with the material. Secondary particles might cross the Cerenkov radiators (gas and quartz) and release light which will be added to the signal of the original primary particle. The trajectory of a secondary particle is typically transverse with respect to the axis of the Cerenkov tube, thus light emission is smaller compared to a primary particle (Figure 8).

11

**Figure 8**. *Path of a secondary particle produced by the interaction of a off-axis primary particle with the tube wall.*

Off-axis primary particles are simulated by shooting 180 GeV pions from the IP with a flat polar angle between 4 and 10 mrad and a flat azimuthal angle between 0 and $2\pi$. The resulting photo-electron spectrum is shown in Figure 9.
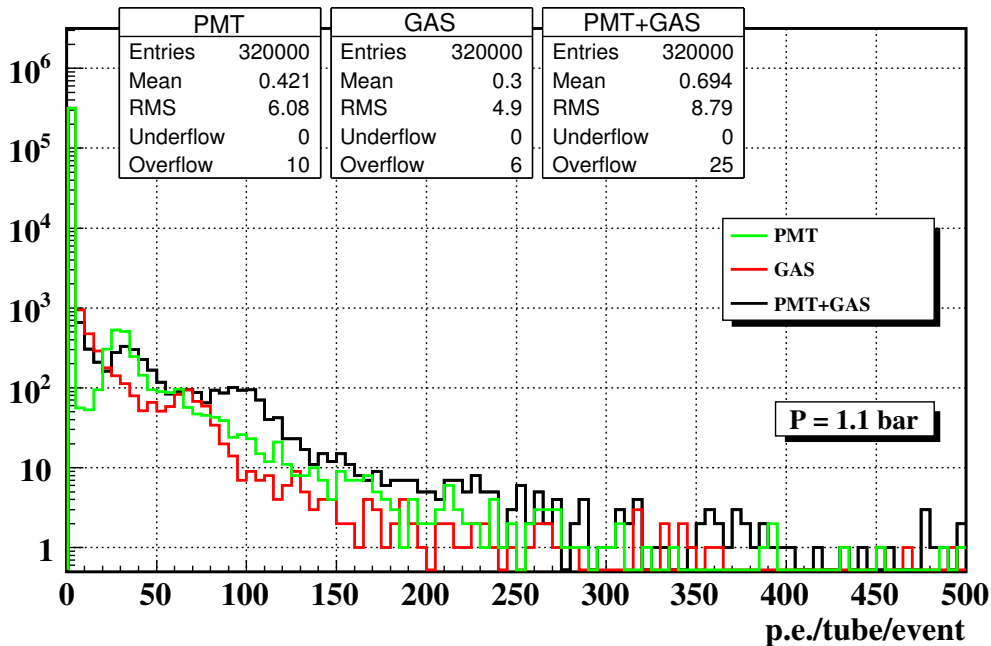


**Figure 9**. *Photo-electrons detected by LUCID in* 10000 *events of single pions coming from the IP with E = 180 GeV and a random direction (0.004 < θ < 0.01, 0 < φ < 2π).*

12

The peak at about 105 photo-electrons is due to on-axis primary particles crossing both Cerenkov radiators (gas and quartz). The peak at 30 photo-electrons originates from secondary particles crossing only the quartz. Compared to Figure 6, a continuous background is created by particles produced in secondary interactions inside LUCID. Even though tube walls are thin ($\approx$ 1 mm), the effective thickness traversed by off-axis primaries is large (about 1.5 m), which results in a large probability for secondary interactions. The effect is only partially suppressed by the smaller path length of secondaries inside the Cerenkov radiator. When the effect of secondary particles is neglected (Figure 10), the photo-electron spectrum of off-axis primaries is similar to that of on-axis primaries (Figure 6).
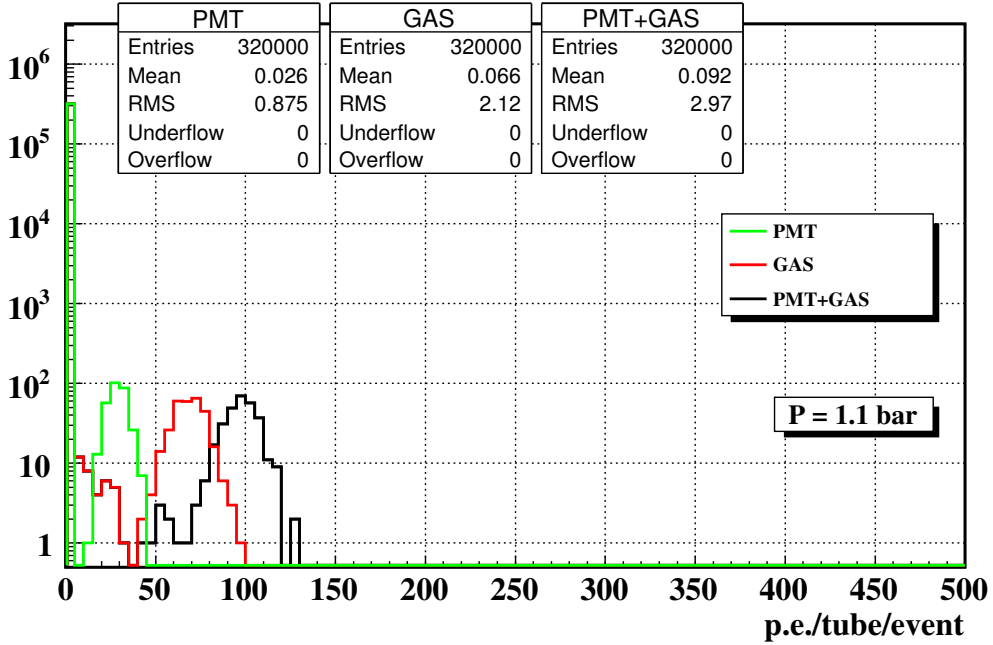


**Figure 10**. *Photo-electrons detected by LUCID in* 10000 *events of single pions coming from the IP with E = 180 GeV and a random direction (0.004 < θ < 0.01, 0 < φ < 2π). Secondary interactions inside the detector material are neglected.*

This is due to the fact that LUCID tubes are so "far" from the IP (about 17 m) that off-axis primary particles are almost parallel to the tube axis, therefore the path inside the radiator of off-axis and on-axis primaries are similar.

## 3.3    Signal from off-axis photons

Neutral particles do not emit Cerenkov photons when crossing the LUCID detector. Still, neutral particles might affect the LUCID response by producing charged particle when interacting with the LUCID tube walls. The spectrum of photo-electrons detected by LUCID due to 100 GeV photons is shown in Figure 11.
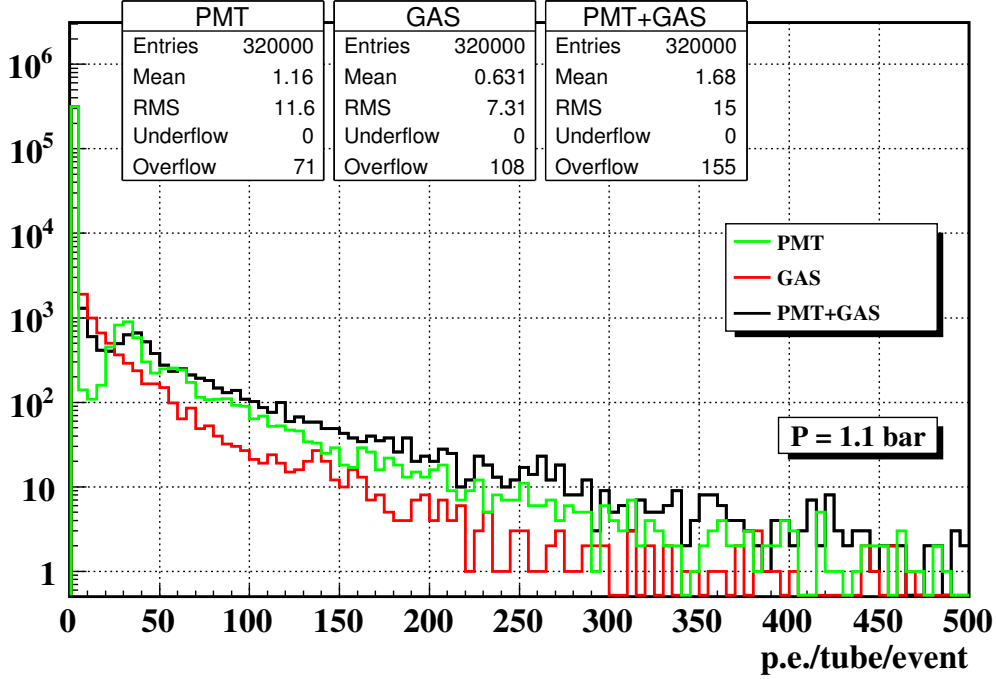
**Figure 11**. *Photo-electrons detected by LUCID in* 10000 *events of single photons coming from the IP with E* = 100 *GeV and a random direction (*$0.004 < \theta < 0.01$*,* $0 < \phi < 2\pi$*).*

The peak at 30 photo-electrons is due to secondary particles crossing the PMT window only. Compared to Figure 10, the peak at about 105 photo-electrons is not visible due to the fact that secondary particles typically do not travel along the tube axis.

# 4   Response to $pp$ collisions

Primary $pp$ collisions at 14 TeV center of mass energy are simulated according to the production cross sections and decay branching ratios provided by PHOJET (version 1.12.1.35) [8]. Particles are fed through a GEANT3-GCALOR [9] simulation of the ATLAS detector in order to describe the interaction of primary particles with the detector material up to the LUCID mother volume (a volume containing the LUCID detector). All primary and secondary particles hitting the LUCID mother volume are finally used as input for the last simulation step in which the LUCID performance is evaluated with the GEANT4 [1] detector simulation illustrated in Section 2. Background originating from beam halo and beam-gas interactions inside the beam pipe is not simulated. The main features of tracks entering the LUCID mother volume are compared to those of tracks detected by LUCID.

## 4.1 Event generator

Several packages are available for the simulation of the physics processes occurring in $pp$ collisions. The difference among them reflects the systematic uncertainty in the models which are used to describe the interaction of protons.

The total $pp$ cross-section can be divided into elastic and inelastic components, and the inelastic component can be further divided into: non-diffractive, single diffractive and double diffractive components [10]. The total cross-section ($\sigma_{tot}$) can then be written as:

$$\sigma_{tot} = \sigma_{el} + \sigma_{sd} + \sigma_{dd} + \sigma_{nd} \tag{11}$$

where these cross-sections are elastic ($\sigma_{el}$), single diffractive ($\sigma_{sd}$), double diffractive ($\sigma_{dd}$) and non-diffractive ($\sigma_{nd}$), respectively. The production cross section of the different inelastic processes predicted by PYTHIA [11] and PHOJET [8] at the center-of-mass energy of 14 TeV are reported in Table 2 (cross sections at 10 TeV are expected to be 10% lower [12]).

| Type of $pp$ collision | $\sigma$ [mb] in PYTHIA | $\sigma$ [mb] in PHOJET |
|---|---|---|
| Non-diffractive | 55 | 69 |
| Single-diffractive | 14 | 11 |
| Double-diffractive | 10 | 4 |
| Total inelastic | 79 | 84 |

**Table 2**. *Cross section of inelastic processes in pp collisions at 14 TeV predicted by PYTHIA and PHOJET. The table and the list of generator settings can be found in [13].*

As far as LUCID is concerned, elastic interactions are neglected because protons scatter at smaller angles and interact further downstream. The pseudo-rapidity of all charged particles produced in single-, double- and non-diffractive processes predicted by PYTHIA and PHOJET are shown in Figure 12 when the pseudo-rapidity region in which LUCID operates is highlighted ($5.6 < \eta < 6.2$).

Although the predictions of the total cross section of PYTHIA and PHOJET are close, the two generators forecasts a different particle multiplicity and a different sharing of event types. There is no ground at present to consider one generator more reliable than the other. The study presented in this note is done with about 9159 events of single $pp$ interactions generated with PHOJET 1.12.1.35 [8] in the full pseudo-rapidity range.
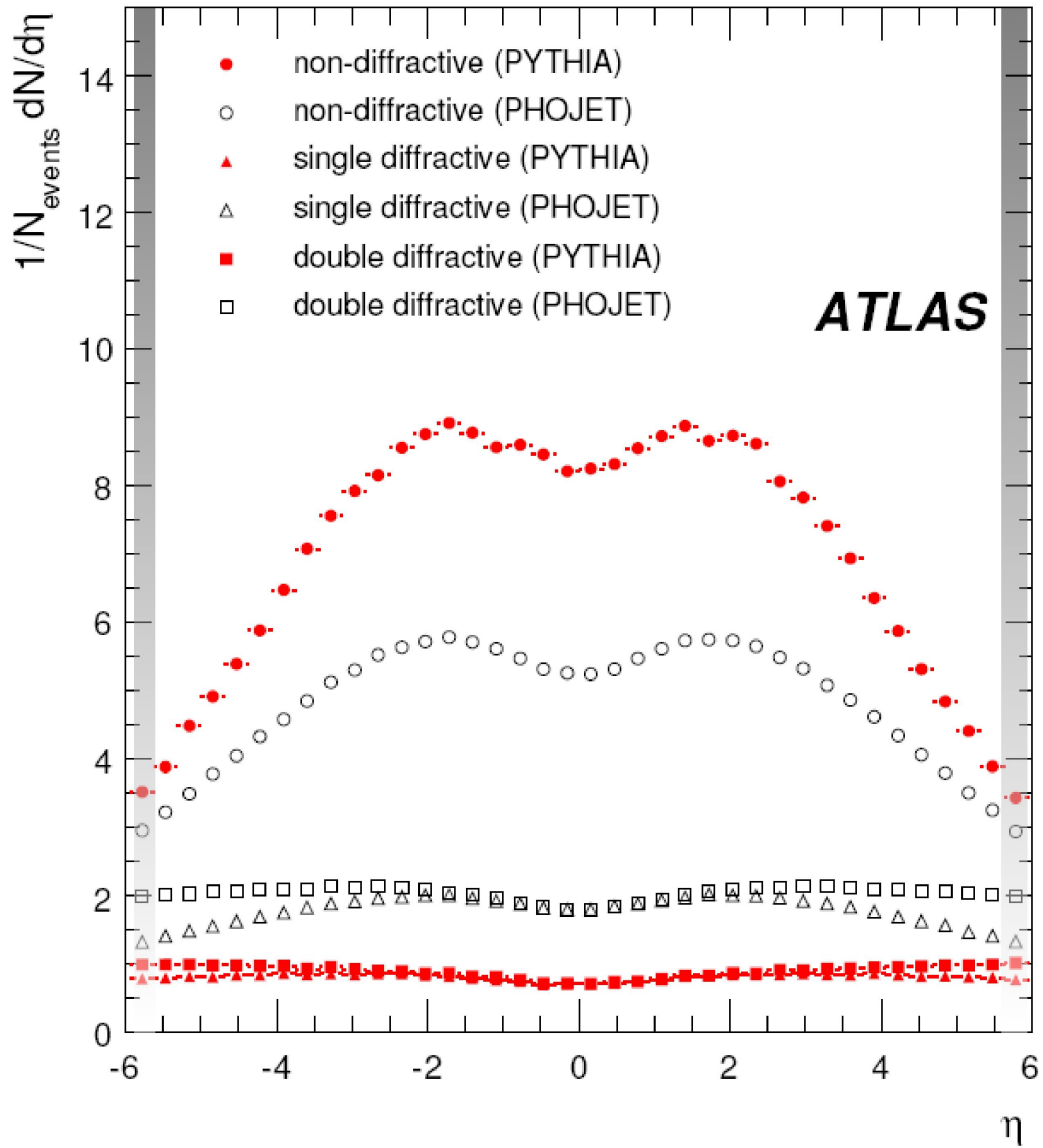
**Figure 12**. *Pseudo-rapidity of stable charged particles in different types of inelastic pp collisions as predicted by PHOJET (open symbols) and PYTHIA (closed symbols) [13]. The region in which LUCID operates (5.6 < η < 6.2) is highlighted.*

## 4.2   Track propagation inside ATLAS

Generated particles are fed through a GEANT3-GCALOR [9] simulation of the ATLAS detector including all sub-systems (magnets, trackers, calorimeters etc.), with the exception of LUCID. The generator settings and detector geometry used in a previous study of radiation background [14] are chosen here due to the particular attention given to low energetic processes, such as electromagnetic showers, which are essential for the study of radiation background.

Being located close to the beam pipe inside the forward muon shielding, LUCID is exposed to a large flux of secondary particles. In fact, primary particles produced by inelastic *pp* collisions interact with the material of the experiment producing secondary particles that may reach LUCID from any direction.

The energy threshold for particle detection in LUCID is such that the effect of secondary particles might be not negligible (only 0.7 MeV for electrons in quartz).

The original idea behind the LUCID design was to build a detector capable of distinguishing between primary and secondary particles. Due to the projective geometry of LUCID, primary particles travel typically longer paths inside a tube compared to secondary particles (Figure 13). Primary particles are therefore expected to emit more Cerenkov light than secondaries.
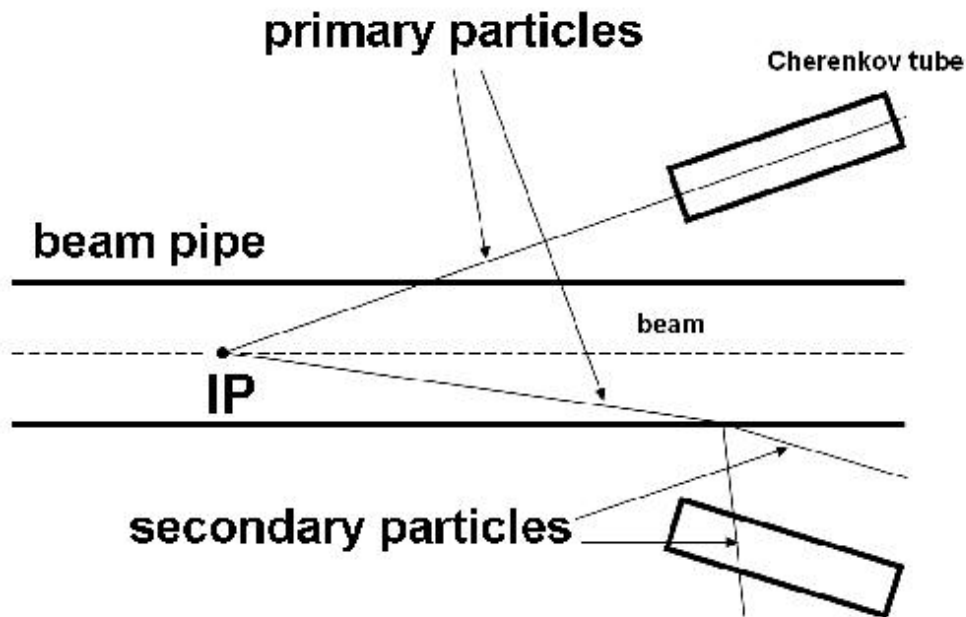


**Figure 13**. *Schematic view of primary and secondary particle path inside LUCID. Here the secondaries are due to the interaction between the primary and the beam pipe.*

## 4.3   The LUCID volume

The LUCID volume is defined around the region where the LUCID tubes are actually located. It has similar dimensions to the external vessel in which the Cerenkov tubes are contained. The position and the four-vectors (energy and momentum) of all particles hitting the surface delimiting this volume is recorded, together with the information of the type and the origin of the particle (primary or secondary). The coordinates of the impact points for a subset of events is shown in Figure 14.
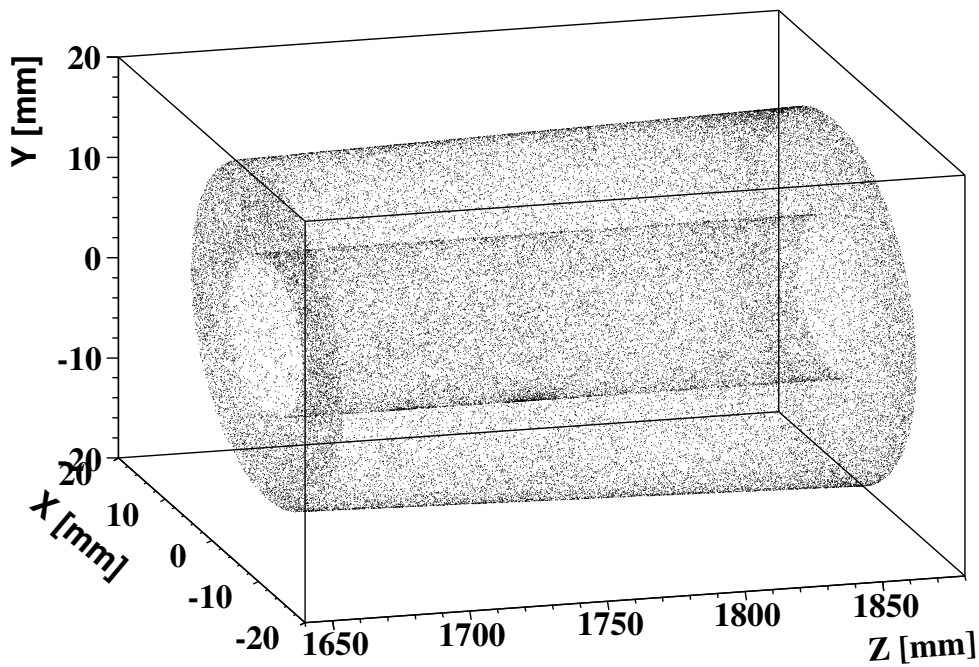


**Figure 14**. *The LUCID volume (the z coordinate is along the beam axis).*

The volume is defined in such a way that it contains LUCID and it does not clashes with the neighborhood ATLAS detector subsystems. One can compare the number of primary and secondary particles reaching the LUCID volume (Figure 15).

Most primary particles (filled grey) are pions. Photons from $\pi^0 \rightarrow \gamma\gamma$ prompt decays are also labeled as primary particles, but most of them are absorbed before reaching LUCID. Secondary particles reaching the LUCID volume (solid line) are mostly electrons and photons from electromagnetic showers, while neutrons are due to back-scattering from the material placed downstream of LUCID.
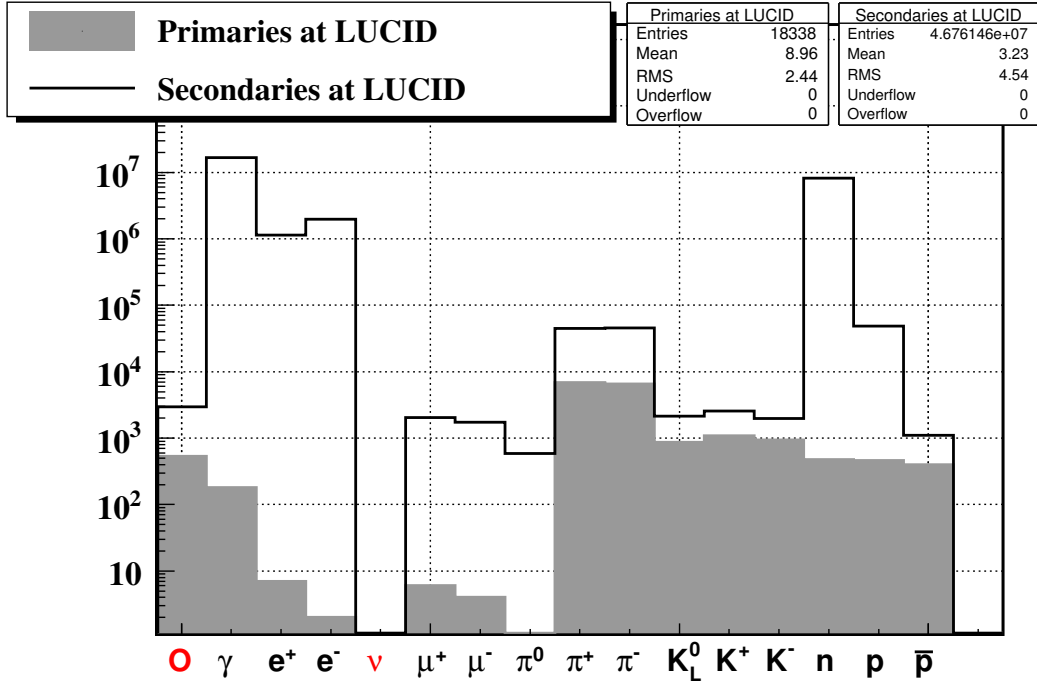
**Figure 15**. *Distribution of primary particles at the IP (dashed line), primary (filled grey) and secondary particles (solid line) at the LUCID volume. The first bin is the overflow.*

## 4.4 Definition of the particle direction

The number of photo-electrons produced by a charged particle crossing a LUCID tube is proportional to the path length inside the Cerenkov radiators (gas and quartz). Particles coming from the interaction point and hitting the LUCID volume on the front side that face the interaction point are expected to travel the longer path inside the tubes and to give a larger contribution of photo-electrons.

In order to study the correlation between the original direction of the particles and the size of the signal inside LUCID, a direction is associated to each particle. The coordinate of the impact point $(x, y, z)$ and the momentum $(p_x, p_y, p_z)$ of primary and secondary particles are used to define a direction for each particle. Three classes are defined: front, side and back. If $z \times p_z < 0$, the particle is defined as "back". If the particle is not "back" and if $|z| > 16601$ mm, the particle is defined as "side". The remaining particles are defined as "front". The $z$ coordinate (the one along the beam axis) of the impact point for the different calsses of particles hitting the LUCID volume is plotted in Figure 16. Of the particles hitting LUCID from the front, only 0.3% are primaries. Most of the particles hitting the LUCID volume are, however, particles coming from the side or the back (85%).

## 4.4 Definition of the particle direction
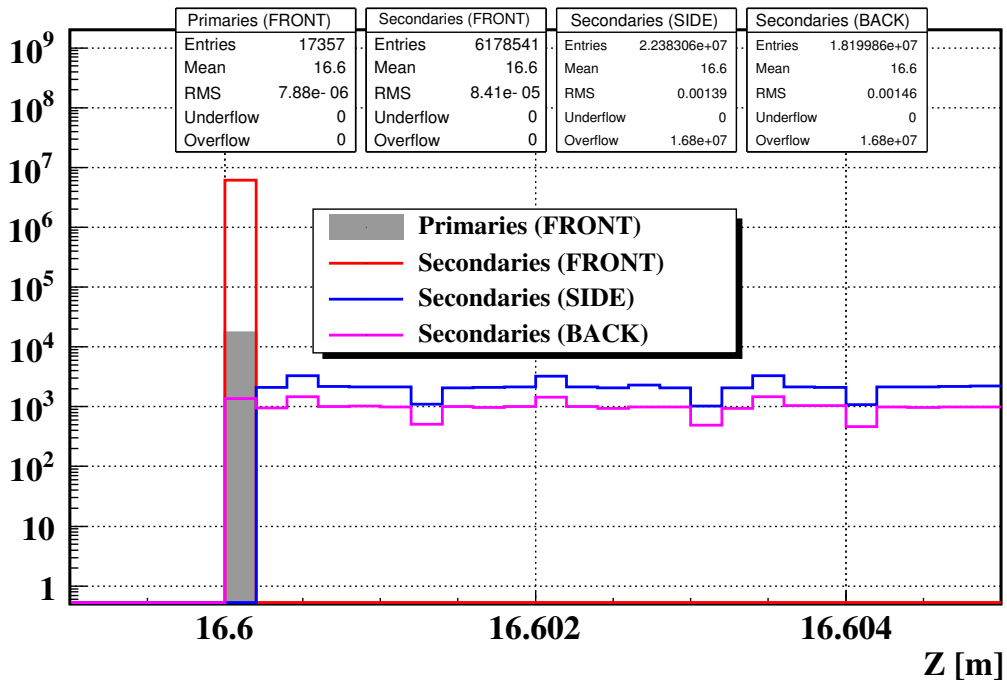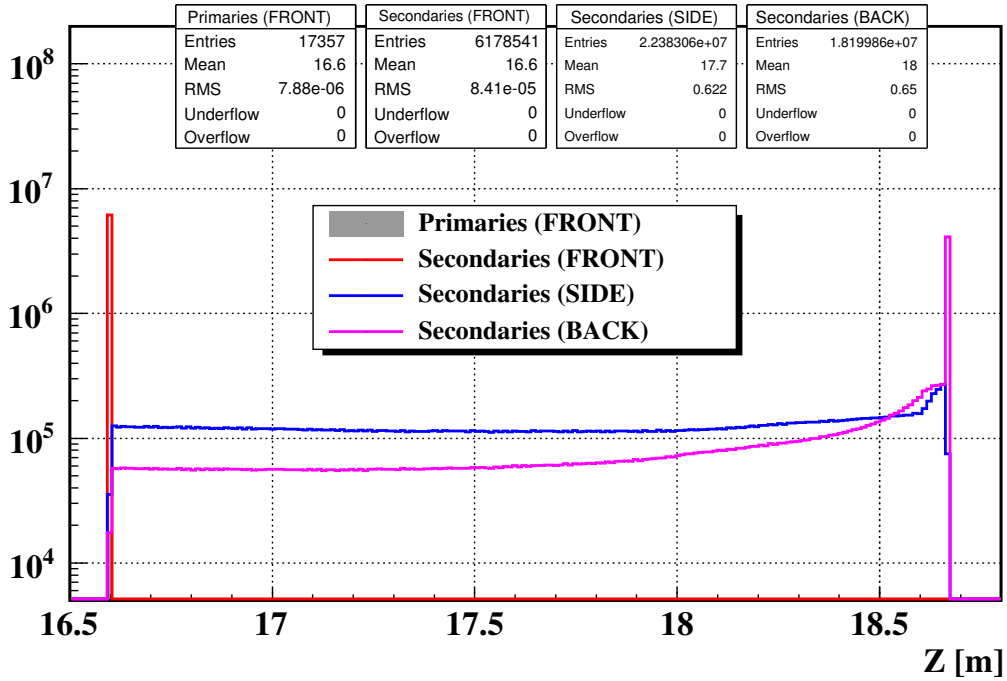


**Figure 16**. *Top: distance from the IP (along the beam axis) of the impact point on LUCID. The results are shown for three classes of particles ("front", "side" and "back"). Bottom: zoom around z = 16.6 m.*

## 4.5   Track propagation inside LUCID

The impact point, the arrival time and the energy at the LUCID volume is used as seed for the track propagation inside the volume with the stand-alone GEANT4 simulation presented in Section 2. One important feature of the analysis presented in this chapter is the traceability of the particles. If a particle generates secondaries inside the LUCID detector material, the release of light due to secondaries is associated to the original track.

## 4.6   Photo-electron spectrum

The response of LUCID to inelastic *pp* collisions in terms of photo-electrons per tube per event is shown in Figure 17.
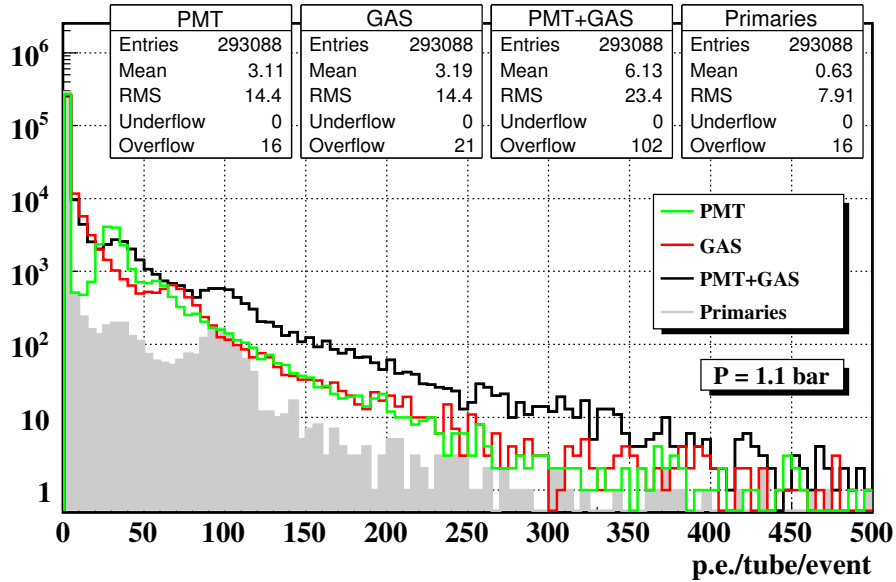


**Figure 17**. *Spectrum of photo-electrons read-out by LUCID in* 9159 *inelastic pp collisions. Contributions from different radiators are shown.*

The photo-electron peaks are at the same positions observed when shooting single particles on LUCID (75 in the gas, 30 in the quartz and 105 in total).

Together with the total number of photo-electrons, Figure 18 shows three contributions: primary particles (grey area), "front" secondaries (red line) and "side" secondaries (green line). Compared to those coming from the "front", "side" secondaries travel a smaller path into the tube, thus releasing less Cerenkov light. Note that the spectrum of primary particles is broad and does not present a sharp peak. This is due to secondary particles produced in the LUCID materials (vessel and tubes) giving small signals, similarly to the case of high energy pions from the IP with a random direction (Figure 9).
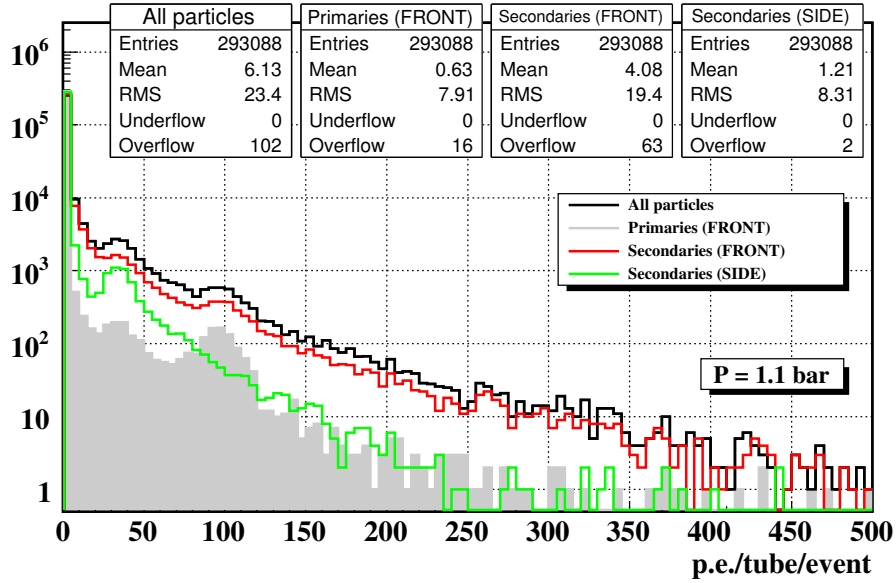
**Figure 18**. *Spectrum of photo-electrons read-out by LUCID in* 9159 *inelastic pp collisions. Contributions of particles having different directions are shown.*

## 4.7 Hit definition

The average number of photo-electrons produced by an on-axis primary particle is about 105 (Figure 6). The largest fraction of secondaries releases light only in the PMT window (30 photo-electrons). A cut-off threshold of 50 photo-electrons allows us to keep the entire signal of primary particles, while suppressing large fraction of secondaries which are not directly correlated with primary particle.

Such a threshold allows one to remove also light detection related effects (dark current and thermo-ionic emission) which are at level of few photo-electrons. The main features of tracks entering the LUCID volume (arrival time, impact angle and energy) are compared to those of tracks detected by LUCID with a signal of at least 50 photo-electrons.

## 4.8 Time of flight

Particles produced by protons colliding at 14 TeV center of mass energy travel approximately at the speed of light inside the ATLAS detector. The time needed by primary particles to cover the distance from the interaction point to the front side of LUCID in a straight line is about 56 ns. For geometrical reasons, the time of arrival of secondaries is expected to be longer since they travel longer paths before hitting the LUCID volume. This is especially true for secondary particles hitting the side or the back of the volume. The time of flight to the LUCID volume of all particles and those which are detected are shown in Figure 19.

| | Primaries (FRONT) | | Secondaries (FRONT) | | Secondaries (SIDE) | | Secondaries (BACK) |
|---|---|---|---|---|---|---|---|
| Entries | 17357 | Entries | 6178541 | Entries | 2.238306e+07 | Entries | 1.819986e+07 |
| Mean | 55.4 | Mean | 55.5 | Mean | 59.8 | Mean | 62.6 |
| RMS | 0.238 | RMS | 1.16 | RMS | 3.6 | RMS | 4.9 |
| Underflow | 0 | Underflow | 0 | Underflow | 0 | Underflow | 0 |
| Overflow | 0 | Overflow | 5.39e+04 | Overflow | 2.73e+06 | Overflow | 5.23e+06 |

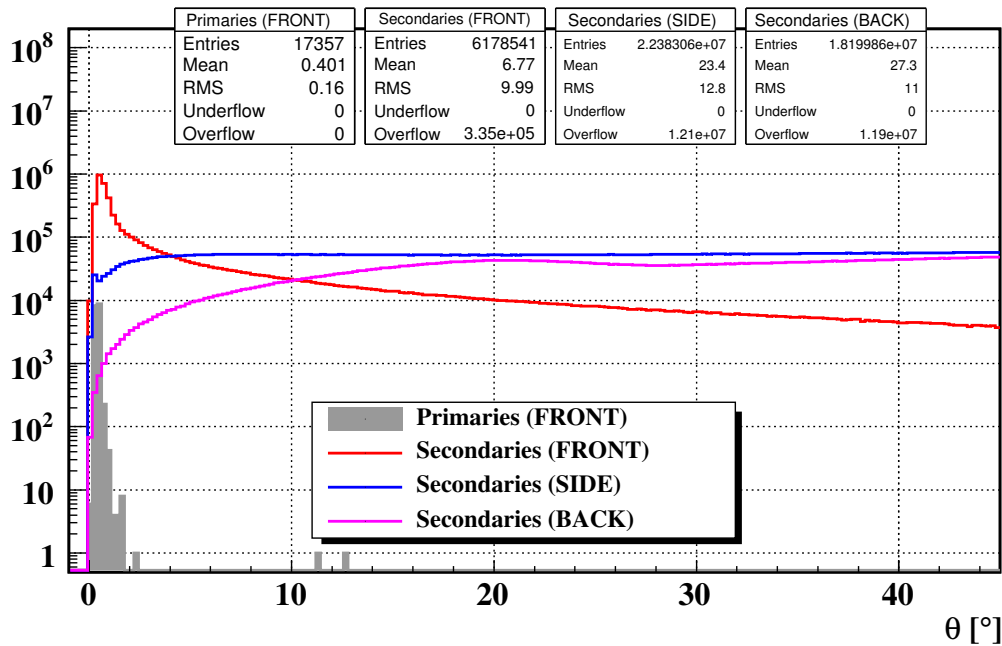| | Primaries (FRONT) | | Secondaries (FRONT) | | Secondaries (SIDE) | | Secondaries (BACK) |
|---|---|---|---|---|---|---|---|
| Entries | 1456 | Entries | 7041 | Entries | 1417 | Entries | 92 |
| Mean | 55.4 | Mean | 55.4 | Mean | 58.9 | Mean | 62.8 |
| RMS | 0.225 | RMS | 0.236 | RMS | 1.73 | RMS | 1.96 |
| Underflow | 0 | Underflow | 0 | Underflow | 0 | Underflow | 0 |
| Overflow | 0 | Overflow | 0 | Overflow | 3 | Overflow | 9 |

**Figure 19**. *Time of arrival to the LUCID volume of all particles (top) and of those which are detected with a* 50 *p.e. threshold (bottom).*

23

Detected "front" secondaries are in time with primaries (within 2 ns) and are about a factor 5 more than primaries. Secondaries from the side are about 20% more than primaries and are spread over a larger range of time due to the shape of the LUCID volume. Detected secondaries from the back are negligible. Detected "side" and "back" secondaries have a peak at about 61 ns, which is the time needed to reach the position of the PMT.

## 4.9    Angle to the beam

Primary and secondary particles detected by LUCID hit almost simultaneously the front face of the LUCID volume. However, secondary particles, being the product of scattering of primary particles through different materials, are expected to travel along different directions with respect to primaries. The angle between the beam axis and the trajectory of primary and secondary particles is shown in Figure 20 for all particles and in Figure 21 for those which are detected.



**Figure 20**. *Angle to the beam of particles crossing the LUCID volume.*

The angle of detected primary particles is less than $1°$ and has an average of $0.35°$. The peaks of "front" and "side" secondaries are at the same position of primaries but distributions are broader (with an average of $0.6°$ and $4.1°$). Secondaries from the "back" have larger angles. Due to the pointing nature of LUCID, secondaries with an angle larger than $2°$ (both "front" and "side") are strongly suppressed when required to give a signal in LUCID.
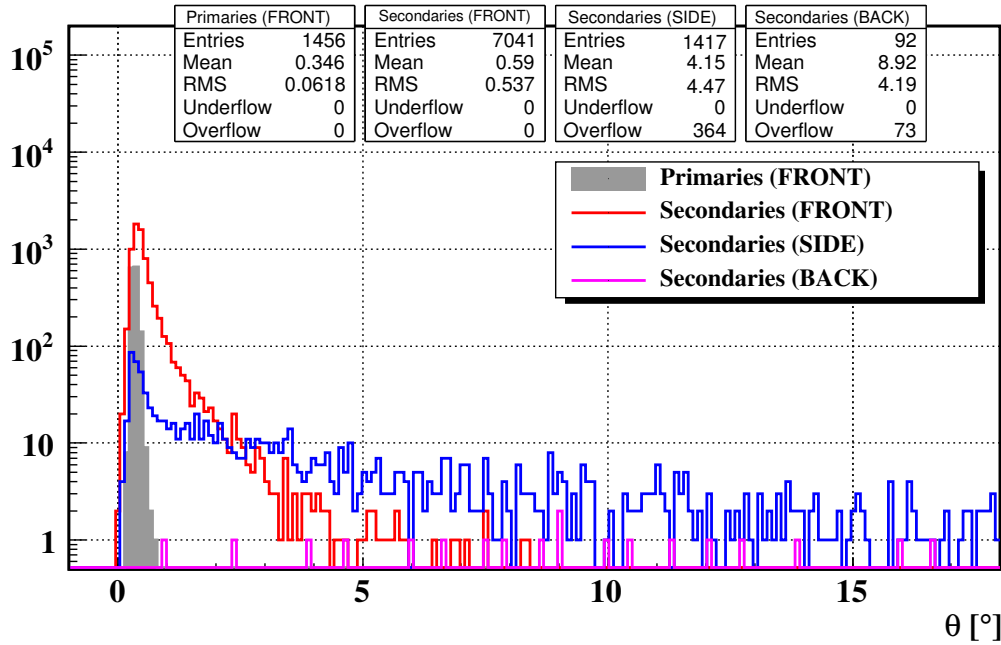
**Figure 21**. *Angle to the beam of particles detected by LUCID with a 50 p.e. threshold.*

## 4.10    Energy

Primary particle are mostly pions, while secondary particles are mostly photons and electrons. Neutral particles don't emit directly Cerenkov light. However, neutral particles crossing the LUCID volume might interact with the LUCID material and produce charge particles (ex: $\gamma \rightarrow e^+e^-$) which undergo Cerenkov effect. This means that, as far as particles at the LUCID volume are concerned, neutral particles still play a role in LUCID. The energy distribution of primary and secondary pions, photons and electrons are shown in Figure 22-Figure **??**.

The requirement of being detected by LUCID suppresses soft particles. The average energy of a detected primary pion is 74 GeV, which is larger than that of secondary pions from the front (46 GeV) and from the side (56 GeV). Pions from the back have much smaller energy (0.4 GeV).

Primary photons and electrons hitting the LUCID volume are few. As for pions, the requirement of being detected by LUCID suppresses the soft part of the energy spectrum. The average energy of a detected "front" secondary photon (electron) is 1 GeV (2 GeV). Most secondary particles from the "back" have an energy smaller than the Cerenkov threshold.

| Primaries (FRONT) | | Secondaries (FRONT) | | Secondaries (SIDE) | | Secondaries (BACK) | |
|---|---|---|---|---|---|---|---|
| Entries | 12700 | Entries | 32861 | Entries | 40997 | Entries | 16564 |
| Mean | 57.9 | Mean | 17.2 | Mean | 2.68 | Mean | 0.331 |
| RMS | 38.1 | RMS | 23.2 | RMS | 8.91 | RMS | 0.185 |
| Underflow | 0 | Underflow | 0 | Underflow | 0 | Underflow | 0 |
| Overflow | 601 | Overflow | 128 | Overflow | 25 | Overflow | 0 |

| Primaries (FRONT) | | Secondaries (FRONT) | | Secondaries (SIDE) | | Secondaries (BACK) | |
|---|---|---|---|---|---|---|---|
| Entries | 1190 | Entries | 782 | Entries | 180 | Entries | 6 |
| Mean | 74 | Mean | 45.7 | Mean | 56 | Mean | 0.408 |
| RMS | 42.3 | RMS | 38 | RMS | 46.2 | RMS | 0.154 |
| Underflow | 0 | Underflow | 0 | Underflow | 0 | Underflow | 0 |
| Overflow | 131 | Overflow | 32 | Overflow | 9 | Overflow | 0 |

**Figure 22**. *Energy distribution of all pions crossing the LUCID volume (top) and of those which are detected by LUCID with a 50 p.e. threshold.*

26

**Figure 23**. *Energy distribution of photons crossing the LUCID volume(top) and of those which are detected by LUCID with a 50 p.e. threshold.*
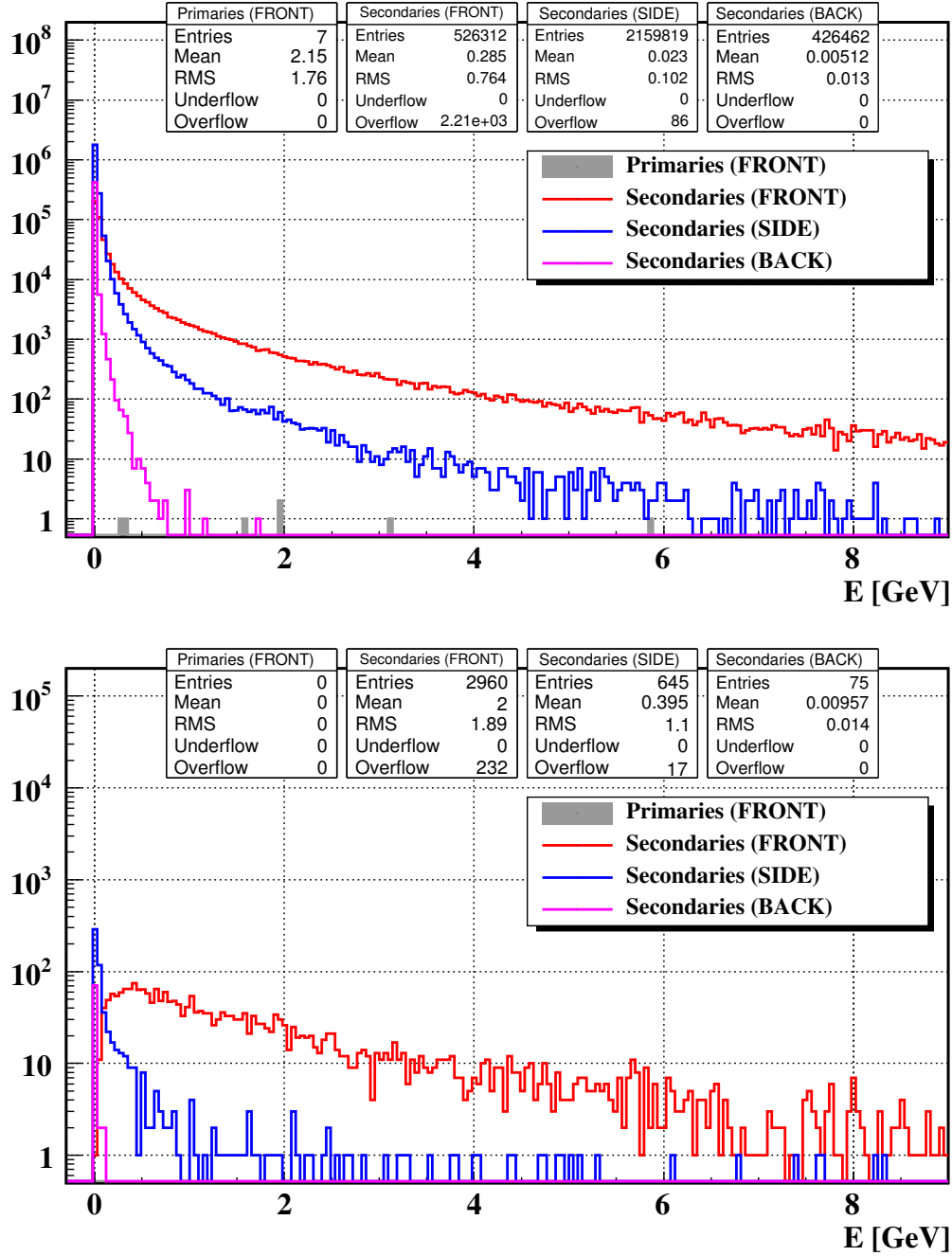
**Figure 24**. *Energy distribution of electrons crossing the LUCID volume (top) and of those which are detected by LUCID with a 50 p.e. threshold.*

# 5 Study of luminosity monitoring algorithms

This section is dedicated to the study of the LUCID performance as a luminosity monitoring system. The Monte Carlo simulation of the full ATLAS detector described in Section 4 is used to simulate the **reference sample** and the **measurement sample**. The reference sample consists of 9159 single $pp$ interaction events. The measurement samples are built by overlapping single $pp$ interactions events according to Poissonian distributions. The average number of $pp$ interactions per event ($\mu_{meas}$) is extracted from the measurement samples at high luminosity with several methods and the result is compared with the true value ($\mu_{true}$).

## 5.1 Definition of the type of detected $pp$ interaction

LUCID consists of two modules placed symmetrically around the ATLAS interaction point. Two criteria to detect a $pp$ collision can be defined: single side mode and coincidence mode. In single side mode, a $pp$ interaction is detected if there is at least one hit in *any module*. In coincidence mode, a $pp$ interaction is detected if there is at least one hit in *each module* (Figure 25).
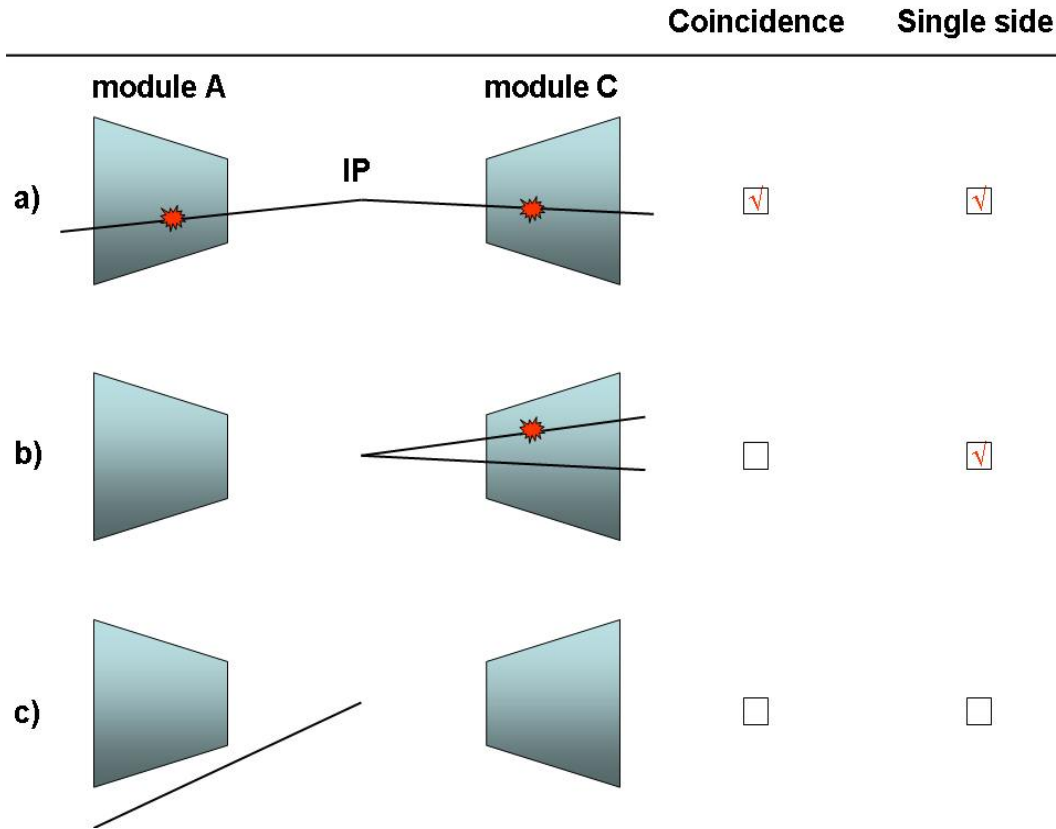


**Figure 25**. *Principle of detection in single side and coincidence modes.*

In a) each module detects a particle. This interaction is detected in single side mode and in coincidence mode. In b) two particles traverse the same module, one of them giving a hit. This interaction is detected in single side mode only. In c) no particle traverses any modules and no interaction is detected.

The advantage of requiring a coincidence is that background produced by beam interactions with residual gas inside the beam pipe or by the beam-halo from the LHC collimators is reduced. Such background is uncorrelated with the ATLAS interaction point and is typically detected in one module only.

## 5.2   Detection efficiency and hit distribution

The detection efficiency and the average number of hits per $pp$ collision are extracted from the reference sample for different criteria used to define a hit. The detection efficiency in single side mode is $\varepsilon^{OR} = (55.8 \pm 0.05)\%$, while that in coincidence mode is $\varepsilon^{AND} = (13.5 \pm 0.4)\%$. The average number of hits per $pp$ collision in single side mode is $N^{OR}_{hits/pp} = 1.21 \pm 0.02$, while that in coincidence mode is $N^{OR}_{hits/pp} = 0.49 \pm 0.01$. The smaller value in coincidence mode is due to the smaller probability of having a hit simultaneously in both modules. Hit multiplicity and tube efficiency are shown in Figure 26 and Figure 27.
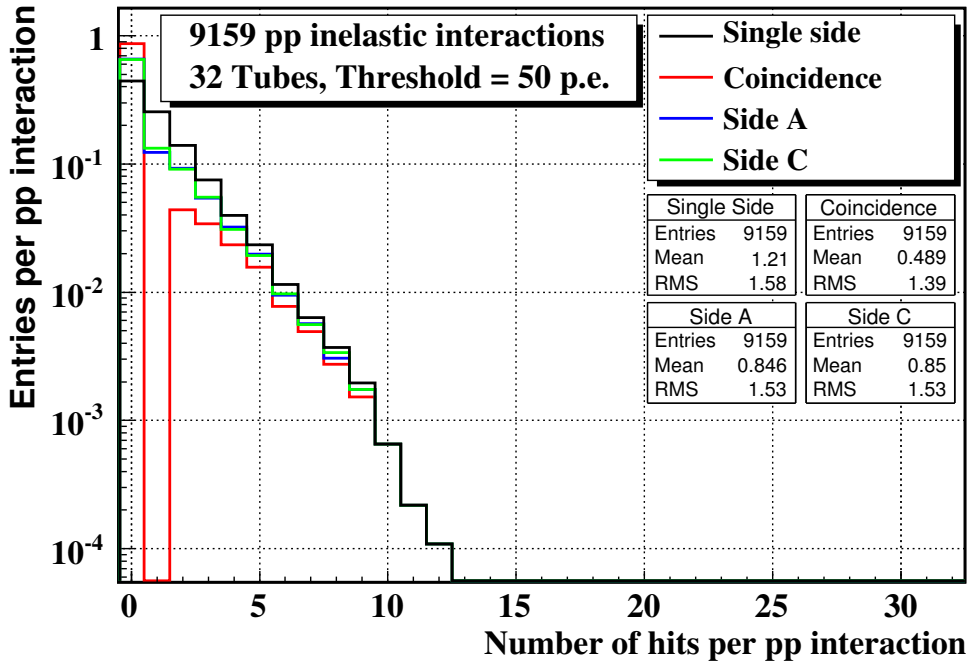


**Figure 26**. *Number of hits per pp interaction with a* 50 *p.e. threshold.*

The probability to have a hit in a tube is approximately the same for all tubes. For tube 0, for instance, the efficiency is $(3.7 \pm 0.2)\%$.
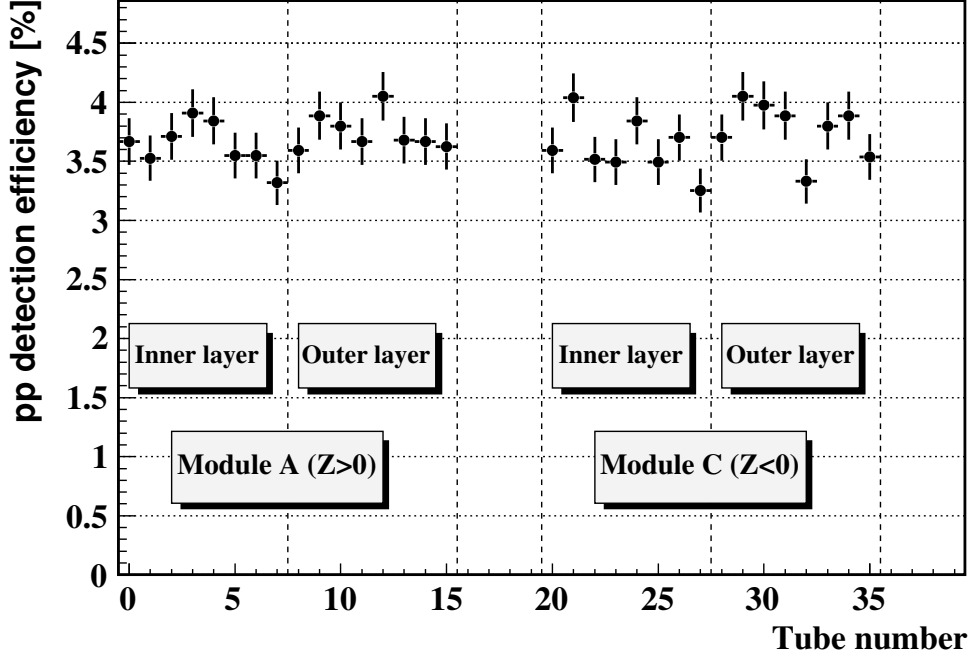
**Figure 27**. *Tube efficiency per pp interaction.*

The number of hits detected in $pp$ interactions can be used to calculate the average number of particles per $pp$ interaction by using Equation 46 in Appendix D.

The efficiency to detect a $pp$ interaction in single side mode ($\varepsilon^{OR}$), coincidence mode ($\varepsilon^{AND}$), in side A ($\varepsilon^A$) and side C ($\varepsilon^A$) and the corresponding average number of hits and particles per $pp$ interaction in the full detector are reported in Table 3.

|  | **Efficiency [%]** | $N_{hits/pp}$ | $N_{part/pp}$ |
|---|---|---|---|
| Single Side | $\varepsilon^{OR} = 55.8 \pm 0.5$ | $N_{hits/pp}^{OR} = 1.21 \pm 0.02$ | $N_{part/pp}^{OR} = 1.27 \pm 0.02$ |
| Coincidence | $\varepsilon^{AND} = 13.5 \pm 0.4$ | $N_{hits/pp}^{AND} = 0.49 \pm 0.01$ | $N_{part/pp}^{AND} = 0.53 \pm 0.02$ |
| Side A | $\varepsilon^{A} = 34.3 \pm 0.5$ | $N_{hits/pp}^{A} = 0.85 \pm 0.02$ | $N_{part/pp}^{A} = 0.90 \pm 0.02$ |
| Side C | $\varepsilon^{C} = 35.0 \pm 0.5$ | $N_{hits/pp}^{C} = 0.85 \pm 0.02$ | $N_{part/pp}^{C} = 0.90 \pm 0.02$ |

**Table 3**. *Efficiency and average number of hits and particles per pp interaction with a 50 p.e. threshold.*

Terms $\varepsilon^A$ and $\varepsilon^A$ are the probability of detecting a $pp$ interaction on one side, regardless of what happens in the other side (they include coincidences). Note that $N_{hits/pp}^{OR}$, $N_{hits/pp}^{A}$ and $N_{hits/pp}^{C}$ are not constrained to be larger than 1 and $N_{hits/pp}^{AND}$ is not constrained to be larger than 2 because the averages are performed on all events, not only on those which are detected.

## 5.3   Simulation of high luminosity events

The measurement samples are built by randomly overlapping single $pp$ interactions according to Poissonian distributions ($0.01 \leq \mu \leq 30$). The overlap is performed by summing up the number of photo-electrons on a tube by tube basis. The photo-electrons distribution for $\mu = 1$ and $\mu = 30$ are shown in Figure 28 and Figure 29. Note that for $\mu = 30$ the signal peak disappears. Due to an increased track multiplicity, the signal peak is hidden by the combinatorial background of secondaries crossing the tubes at large angles and giving small signals (**migration effect**). The average number of hits per event in all measurement samples are reported in Table 4.

| $\mu$ [nm] | $N^{OR}_{hits/BX}$ (thr. = 50 p.e.) | $\mu$ [nm] | $N^{OR}_{hits/BX}$ (thr. = 50 p.e.) |
|---|---|---|---|
| 0.01 | $0.01128 \pm 0.00020$ | 4.00 | $5.19179 \pm 0.08589$ |
| 0.02 | $0.02358 \pm 0.00041$ | 5.00 | $6.65156 \pm 0.10562$ |
| 0.04 | $0.04861 \pm 0.00083$ | 6.00 | $7.93578 \pm 0.12618$ |
| 0.06 | $0.07204 \pm 0.00125$ | 7.00 | $9.37385 \pm 0.14694$ |
| 0.08 | $0.09591 \pm 0.00164$ | 8.00 | $10.33654 \pm 0.16088$ |
| 0.10 | $0.12222 \pm 0.00209$ | 9.00 | $11.95379 \pm 0.17361$ |
| 0.15 | $0.17914 \pm 0.00309$ | 10.00 | $13.12896 \pm 0.19062$ |
| 0.20 | $0.24365 \pm 0.00418$ | 11.00 | $14.22957 \pm 0.20025$ |
| 0.30 | $0.35660 \pm 0.00621$ | 12.00 | $15.22149 \pm 0.21169$ |
| 0.40 | $0.49976 \pm 0.00853$ | 13.00 | $16.35227 \pm 0.22473$ |
| 0.50 | $0.60307 \pm 0.01044$ | 14.00 | $17.68043 \pm 0.22687$ |
| 0.60 | $0.73875 \pm 0.01265$ | 15.00 | $18.71475 \pm 0.22431$ |
| 0.70 | $0.87756 \pm 0.01505$ | 16.00 | $19.49825 \pm 0.23779$ |
| 0.80 | $1.01048 \pm 0.01714$ | 17.00 | $20.36245 \pm 0.24596$ |
| 0.90 | $1.10741 \pm 0.01935$ | 18.00 | $21.50591 \pm 0.23775$ |
| 1.00 | $1.25494 \pm 0.02159$ | 19.00 | $21.94813 \pm 0.23688$ |
| 1.10 | $1.40704 \pm 0.02368$ | 20.00 | $22.79650 \pm 0.23423$ |
| 1.20 | $1.53053 \pm 0.02601$ | 22.00 | $24.07692 \pm 0.22642$ |
| 1.30 | $1.62498 \pm 0.02791$ | 24.00 | $25.37008 \pm 0.23095$ |
| 1.40 | $1.71415 \pm 0.02973$ | 26.00 | $26.78125 \pm 0.21149$ |
| 1.50 | $1.90092 \pm 0.03227$ | 28.00 | $27.67584 \pm 0.18816$ |
| 2.00 | $2.56497 \pm 0.04433$ | 30.00 | $28.19344 \pm 0.18318$ |
| 3.00 | $3.77858 \pm 0.06472$ | | |

**Table 4**. *Average number of hits per event in single side mode for* $0.01 \leq \mu \leq 30$.

The full hit distribution for $\mu = 1$ and $\mu = 30$ are shown in Figure 30 and Figure 31. Due to an increased track multiplicity, the hit distributions in single side and coincidence modes becomes identical at $\mu = 30$.
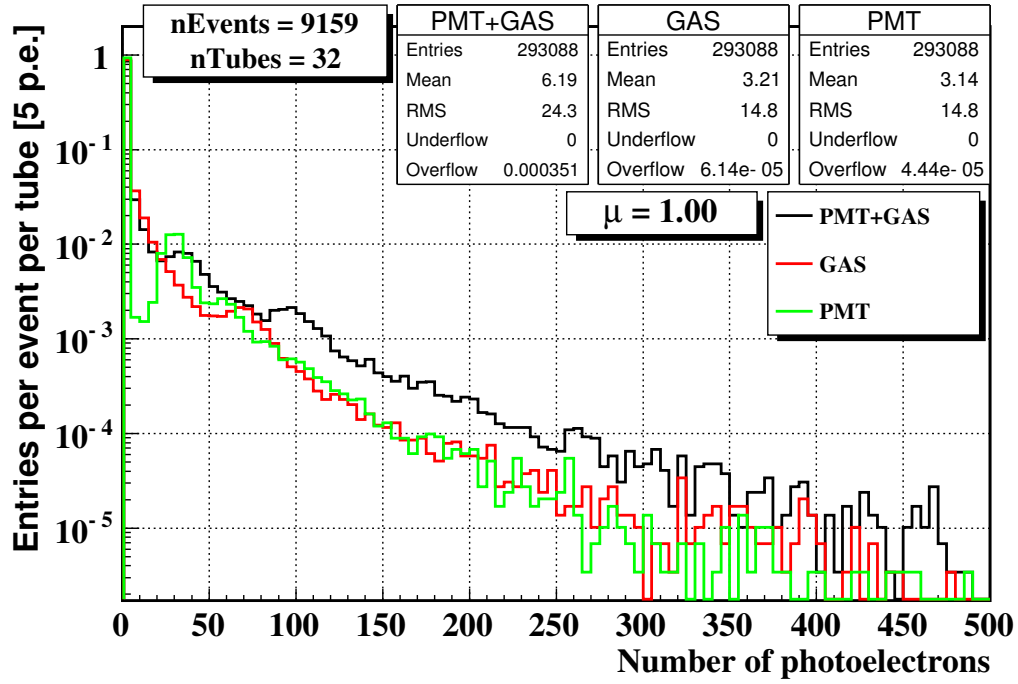
**Figure 28**. *Photo-electron yield from different radiators when μ = 1.*
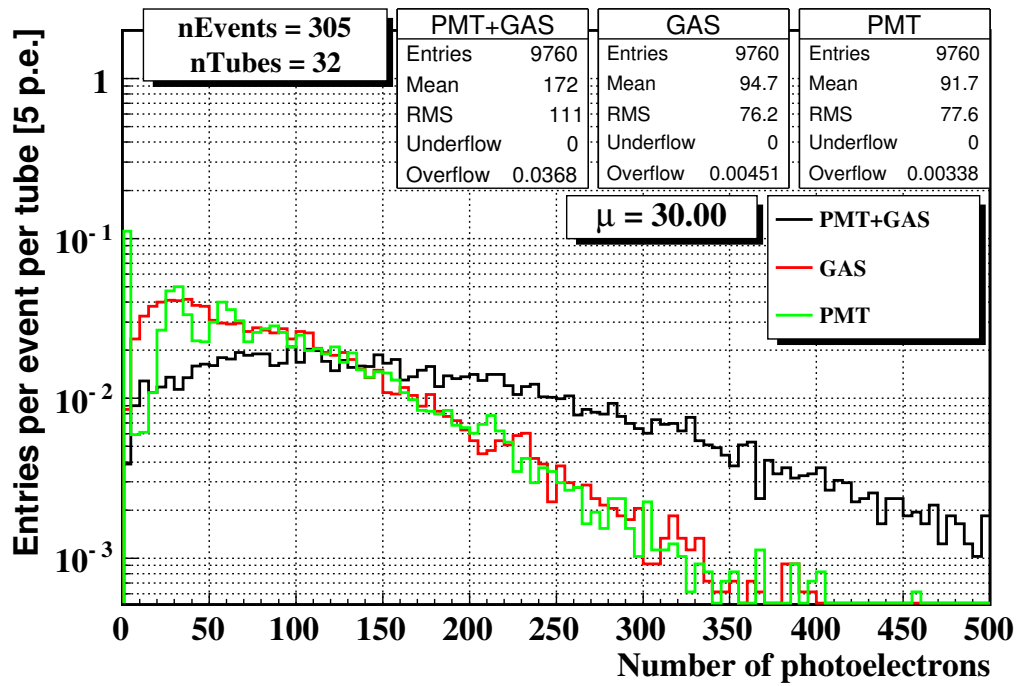


**Figure 29**. *Photo-electron yield from different radiators when μ = 20.*
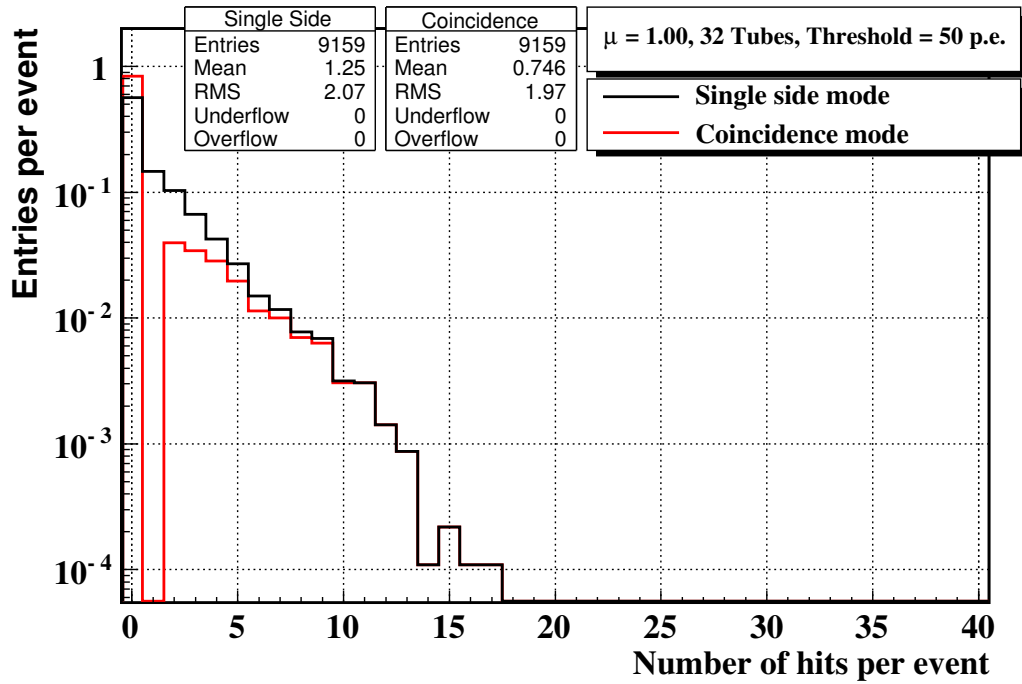
## 5.3 Simulation of high luminosity events



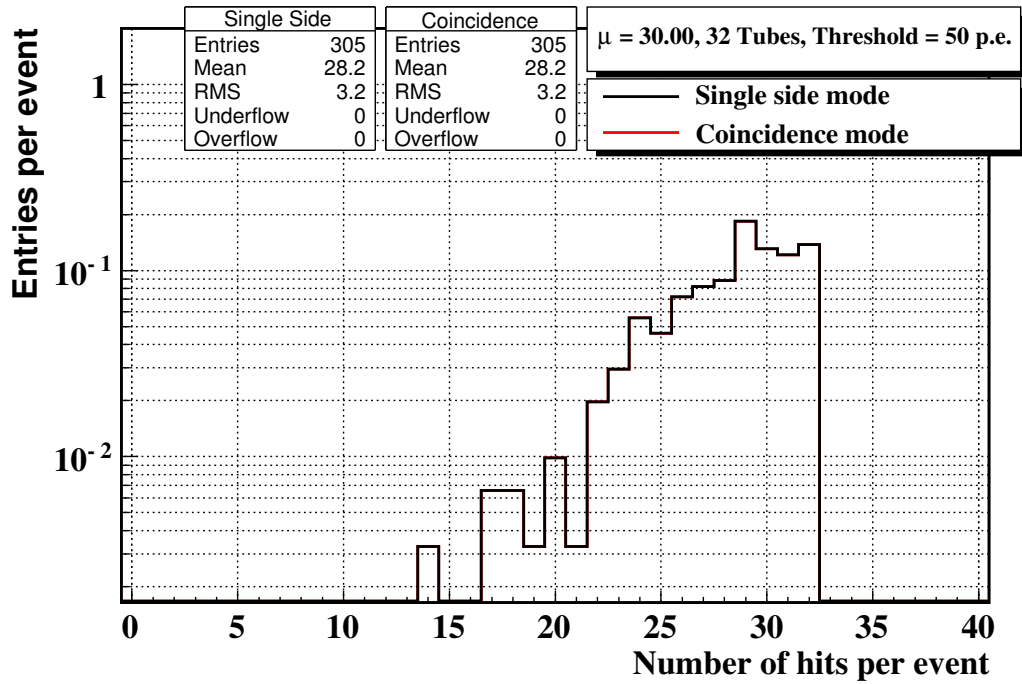**Figure 30**. *Hit distributions with a* 50 *p.e. threshold for* μ = 1.



**Figure 31**. *Hit distributions with a* 50 *p.e. threshold for* μ = 30.

## 5.4 Counting methods

The average number of $pp$ interactions per event ($\mu_{meas}$) is extracted from the high luminosity samples with several methods.

With the **event counting** method $\mu$ is extracted from the rate of detected events. In coincidence mode, events are detected when there is at least one hit in each module ($P^{AND}_{hits/BX}$). In single side mode, detected events have at least one hit in any module ($P^{OR}_{0/BX}$). A method which is statistically equivalent to the event counting is called **zero counting** and consists in counting empty events ($P_{0/BX}$) rather than those with hits ($P_{hits/BX}$).

With the **hit counting** method, $\mu$ is extracted from the number of hits per event. In single side mode, all hits are counted ($N^{OR}_{hits/BX}$). In coincidence mode, hits are counted only in case of simultaneous activity in both detector modules ($N^{AND}_{hits/BX}$). The counting methods are summarized in Table 5.

| measured quantity | side A | side C | name |
|---|---|---|---|
| $P^{OR}_{hits/BX}$ | $N_{hits} \geq 1$ | $N_{hits} \geq 1$ | event counting "OR" |
| | $N_{hits} = 0$ | $N_{hits} \geq 1$ | |
| | $N_{hits} \geq 1$ | $N_{hits} = 0$ | |
| $P^{AND}_{hits/BX}$ | $N_{hits} \geq 1$ | $N_{hits} \geq 1$ | event counting "AND" |
| $P^{OR}_{0/BX} = 1 - P^{AND}_{hits/BX}$ | $N_{hits} = 0$ | $N_{hits} = 0$ | zero counting "OR" |
| | $N_{hits} = 0$ | $N_{hits} \geq 1$ | |
| | $N_{hits} \geq 1$ | $N_{hits} = 0$ | |
| $P^{AND}_{0/BX} = 1 - P^{OR}_{hits/BX}$ | $N_{hits} = 0$ | $N_{hits} = 0$ | zero counting "AND" |
| $N^{OR}_{hits/BX}$ | $N_{hits} \geq 1$ | $N_{hits} \geq 1$ | hit counting "OR" |
| | $N_{hits} = 0$ | $N_{hits} \geq 1$ | |
| | $N_{hits} \geq 0$ | $N_{hits} = 0$ | |
| $N^{AND}_{hits/BX}$ | $N_{hits} \geq 1$ | $N_{hits} \geq 1$ | hit counting "AND" |

**Table 5**. *Counting methods.*

The event counting method has the advantage of relyng on counting events rather than hits. A drawback of this method is that the event rate saturates much faster compared to the hit rate when the luminosity increases, especially for detectors with a large acceptance. At design luminosity ($L = 10^{34}\ cm^{-2}s^{-1}$), the average number of $pp$ interactions per event is 25, which implies a rate of empty events of $e^{-25} \times 40$ MHz $= 5.6 \times 10^{-4}$ Hz (40 MHz is the crossing rate). In case of LUCID, a possible solution is to reduce the detection efficiency by reducing the number of tubes.

Note that hit counting is equivalent to event counting at the level of the single tube, the result being the average on all tubes.

## 5.5 Combinatorial model

The response of LUCID in the measurement samples for both event and hit counting methods are analytically computed by using the information extracted from the reference sample in a combinatorial approach (Appendix B, C, D and E). For each measurement sample ($0.01 \leq \mu \leq 30$), the response of LUCID is used to extract the average number of $pp$ interactions per event ($\mu_{meas}$) and the result is compared with the true value ($\mu_{true}$).

### 5.5.1 Event counting "OR"

With the event counting "OR" method, detected events have at least one hit in a detector module (side A or side C). The average number of $pp$ interactions per event is related to the rate of detected events and to the detection efficiency ($\varepsilon^{OR}$, see Table 3) by Equation 29 of Appendix B:

$$\mu = -\frac{\log(1 - P^{OR}_{hits/BX})}{\varepsilon^{OR}} \tag{12}$$

The measurements of $\mu$ as a function of the true values with the combinatorial model are plotted in Figure 32. The uncertainty on the efficiency is neglected. For $\mu < 5$, the difference between the measured and the true number of $pp$ interactions with two different thresholds (40 and 50 p.e.) is within the statistical uncertainty. For $\mu > 5$ the method suffers from a **saturation effect**. The saturation effect in event counting arises from the fact that at a sufficiently high luminosity all events are detected. Therefore, even though luminosity increases, the response of the detector remains constant and luminosity is underestimated.

**Linear approximation**

For $\mu \ll 1$, $\mu$ is proportional to the rate of detected events ($P^{OR}_{hits/BX}$):

$$\mu \xrightarrow{\mu \ll 1} \frac{P^{OR}_{hits/BX}}{\varepsilon^{OR}} \tag{13}$$

The measurements of $\mu$ as a function of the true values with a linear extrapolation of $P^{OR}_{hits/BX}$ from $\mu = 0.01$ are plotted in Figure 33. A linear fit to the measured points up to $\mu_{true} = 0.1$ has a slope consistent with 1 and is consistent with going through the origin. This means that the measurement of $\mu$ with the linear approximation is reliable up to $\mu = 0.1$. For larger $\mu$ values, $\mu$ is systematically underestimated for two reasons. The saturation effect dominates at $\mu > 5$, when the rate of detected events becomes flat. For intermediate $\mu$ values, $\mu$ is underestimated due to the linear approximation of the logarithm dependence of $P^{OR}_{hits/BX}$ on $\mu$.

Note that just the by taking into account the logarithmic correction, the validity of the method is extended from $\mu = 0.1$ up to $\mu = 5$.
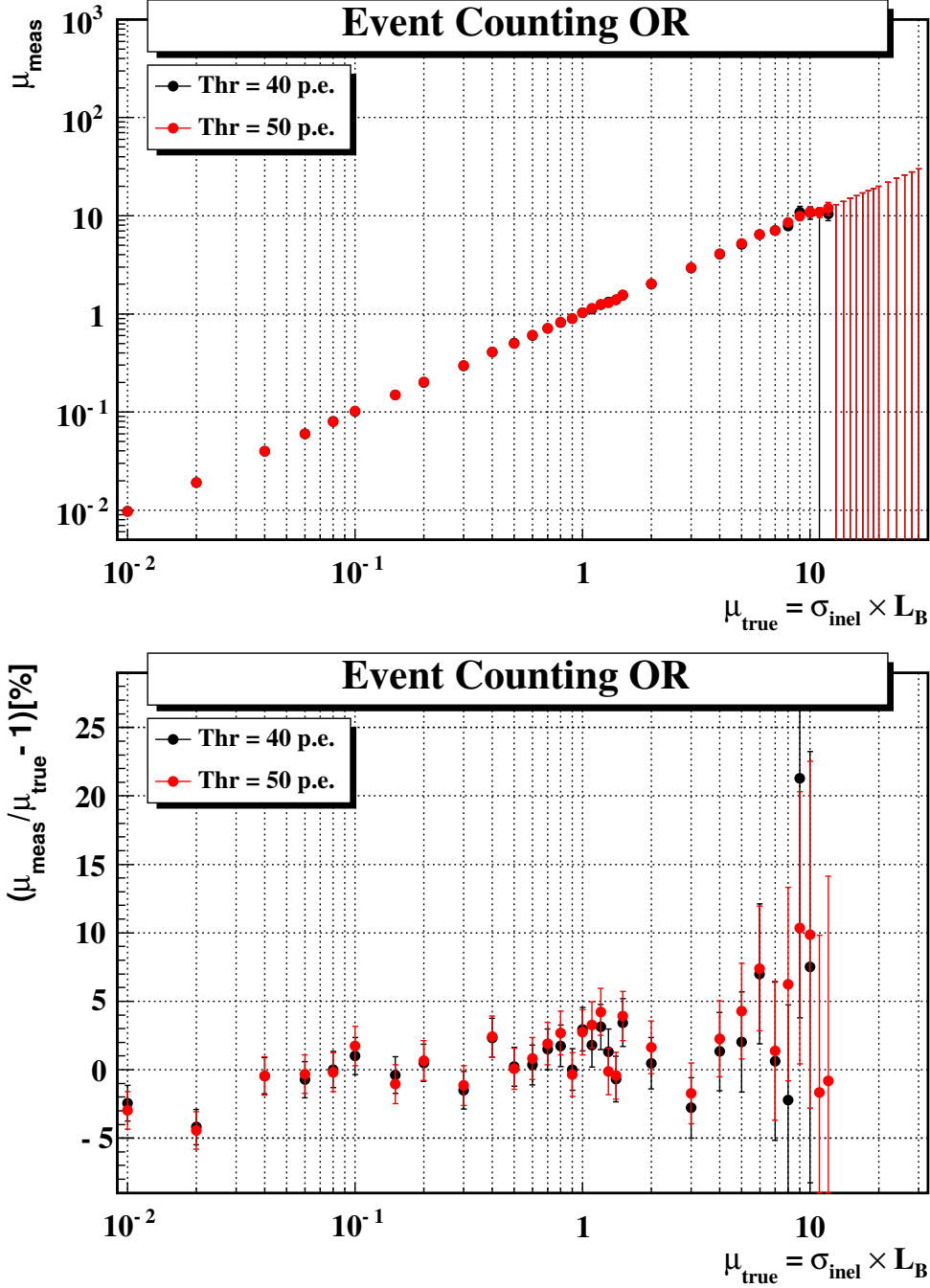
**Figure 32**. *Top: average number of pp interactions per event measured with the event counting "OR" method as a function of the true value for two different thresholds (40 and 50 p.e.). The logarithmic correction given by the combinatorial model is included. Bottom: deviation from the true value.*
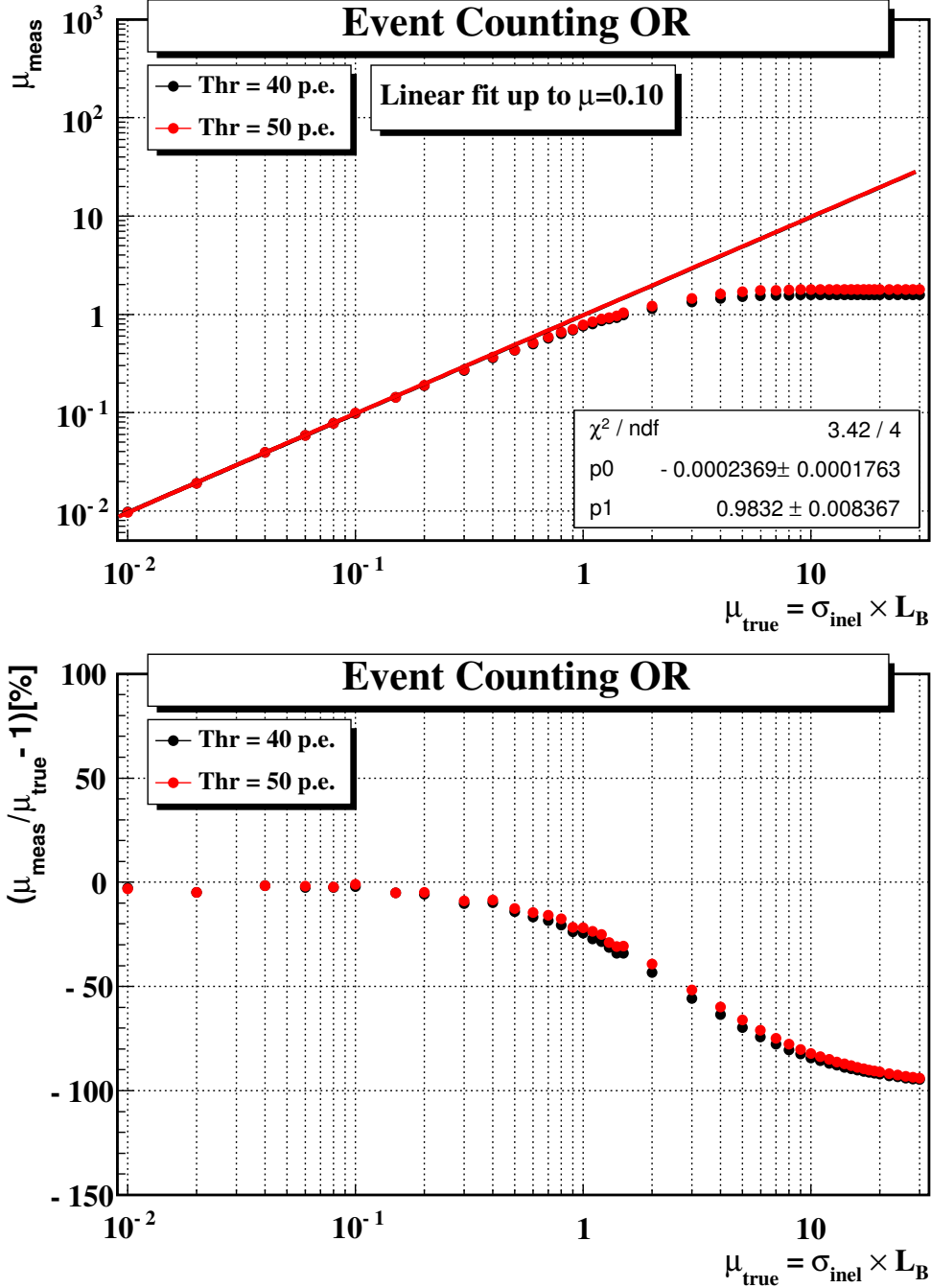
**Figure 33**. *Top: average number of pp interactions per event measured with a linear extrapolation of $P^{OR}_{hits/BX}$ from $\mu = 0.01$ for two different thresholds (40 and 50 p.e.). Bottom: deviation from the true value.*

## 5.5 Combinatorial model

### 5.5.2 Event counting "AND"

With the event counting "AND" method, detected events have at least one hit in each module (side A and side C). The average number of $pp$ interactions per event is related to the rate of detected events and to the detection efficiencies by Equation 41 of Appendix C:

$$P_{hits/BX}^{AND}(\mu) = f(\mu) = 1 - e^{-\mu\varepsilon^A} - e^{-\mu\varepsilon^C} + e^{-\mu(\varepsilon^A + \varepsilon^C - \varepsilon^{AND})} \tag{14}$$

The detection efficiencies ($\varepsilon^A$, $\varepsilon^C$ and $\varepsilon^{AND}$) can be found in Table 3. This equation cannot be inverted analytically, therefore the average number of $pp$ interactions per event is obtained by numerical inversion with a $10^{-10}$ precision:

$$\mu = f^{-1}(P_{hits/BX}^{AND}) \tag{15}$$

The measurements of $\mu$ as a function of the true values with the combinatorial model are plotted in Figure 34. The uncertainty on $\mu$ is the maximum variation of $\mu$ corresponding to a $\pm 1$ $\sigma$ variation of $P_{hits/BX}^{AND}$. The uncertainty on the efficiencies is neglected. With two different thresholds (40 and 50 p.e.), the difference between the measured and the true number of $pp$ interactions is within the statistical uncertainty when $\mu < 5$, while for $\mu > 5$ the prediction deviates from the true value. Due to the migration effect (Section 5.3), the detection efficiency increases with $\mu$, therefore the number of detected events is larger than the prediction and $\mu$ is overestimated.

**Linear approximation**

When $\mu$ is sufficiently small ($\mu \ll 1$), combinatorial effects are negligible and the rate of detected events is proportional to the efficiency:

$$\mu \xrightarrow{\mu \ll 1} \frac{P_{hits/BX}^{AND}}{\varepsilon^{AND}} \tag{16}$$

The measurements of $\mu$ as a function of the true values with a linear extrapolation of $P_{hits/BX}^{AND}$ from $\mu = 0.01$ are plotted in Figure 35. A linear fit to the measured points up to $\mu_{true} = 0.3$ has a slope consistent with 1 and is consistent with going through the origin. This means that the measurement of $\mu$ with the linear approximation is reliable up to $\mu = 0.3$. For larger $\mu$ values, $\mu$ is systematically underestimated for three reasons. The saturation effect dominates at $\mu > 10$, when the rate of detected events becomes flat. For intermediate $\mu$ values, $\mu$ is underestimated due to the linear approximation o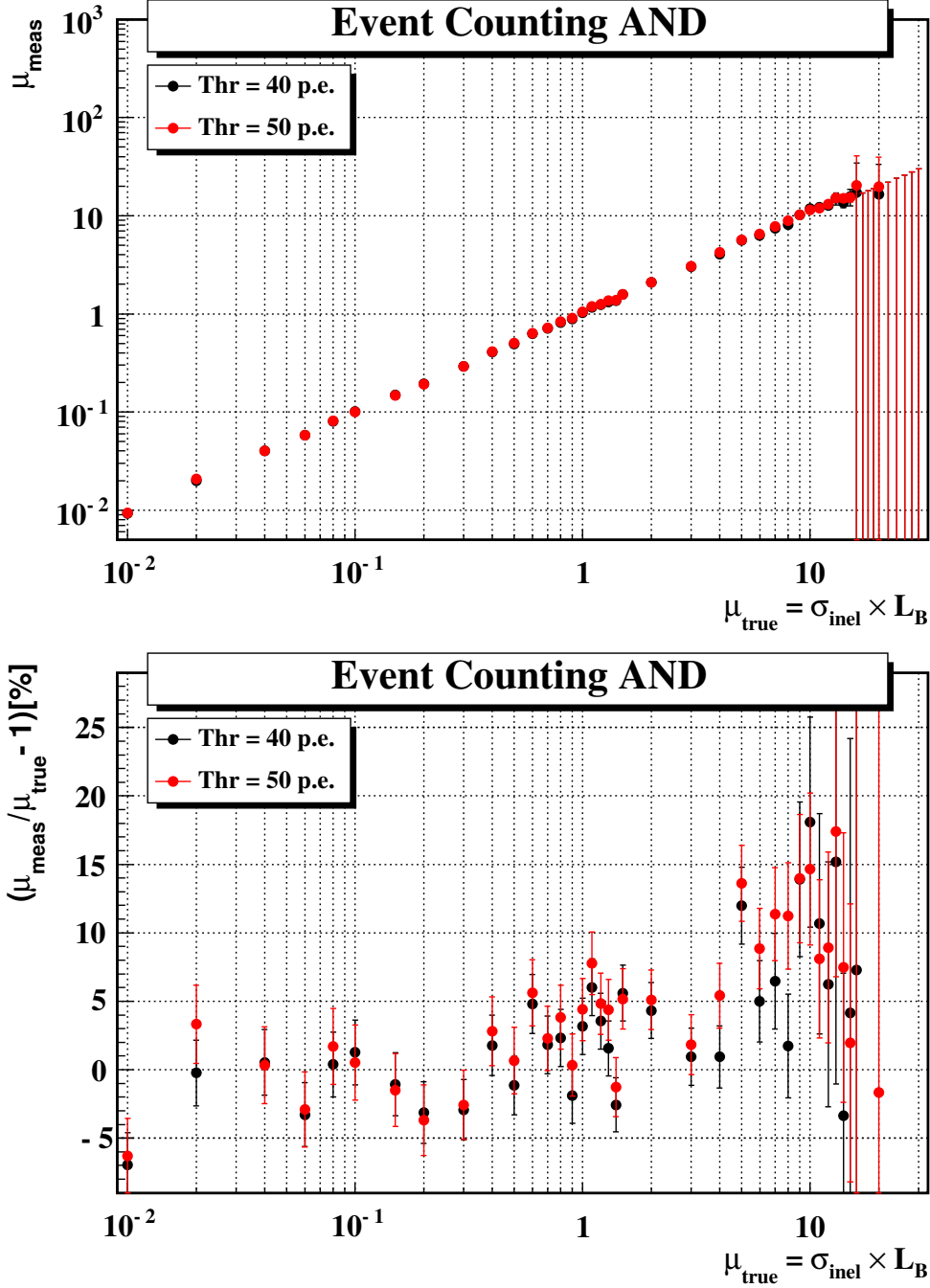f the logarithm dependence of $P_{hits/BX}^{AND}$ on $\mu$ and to the migration effect (Section 5.3). The total effect with a 50 $p.e.$ threshold is about 20% already at $\mu = 1$.

Note that the prediction of the combinatorial model with the event counting "AND" method is as accurate as the event counting "OR" method up to $\mu = 5$.

**Figure 34**. *Top: average number of pp interactions per event measured with the event counting "AND" method as a function of the true value for two different thresholds (40 and 50 p.e.). The logarithmic correction given by the combinatorial model is included. Bottom: deviation from the true value.*
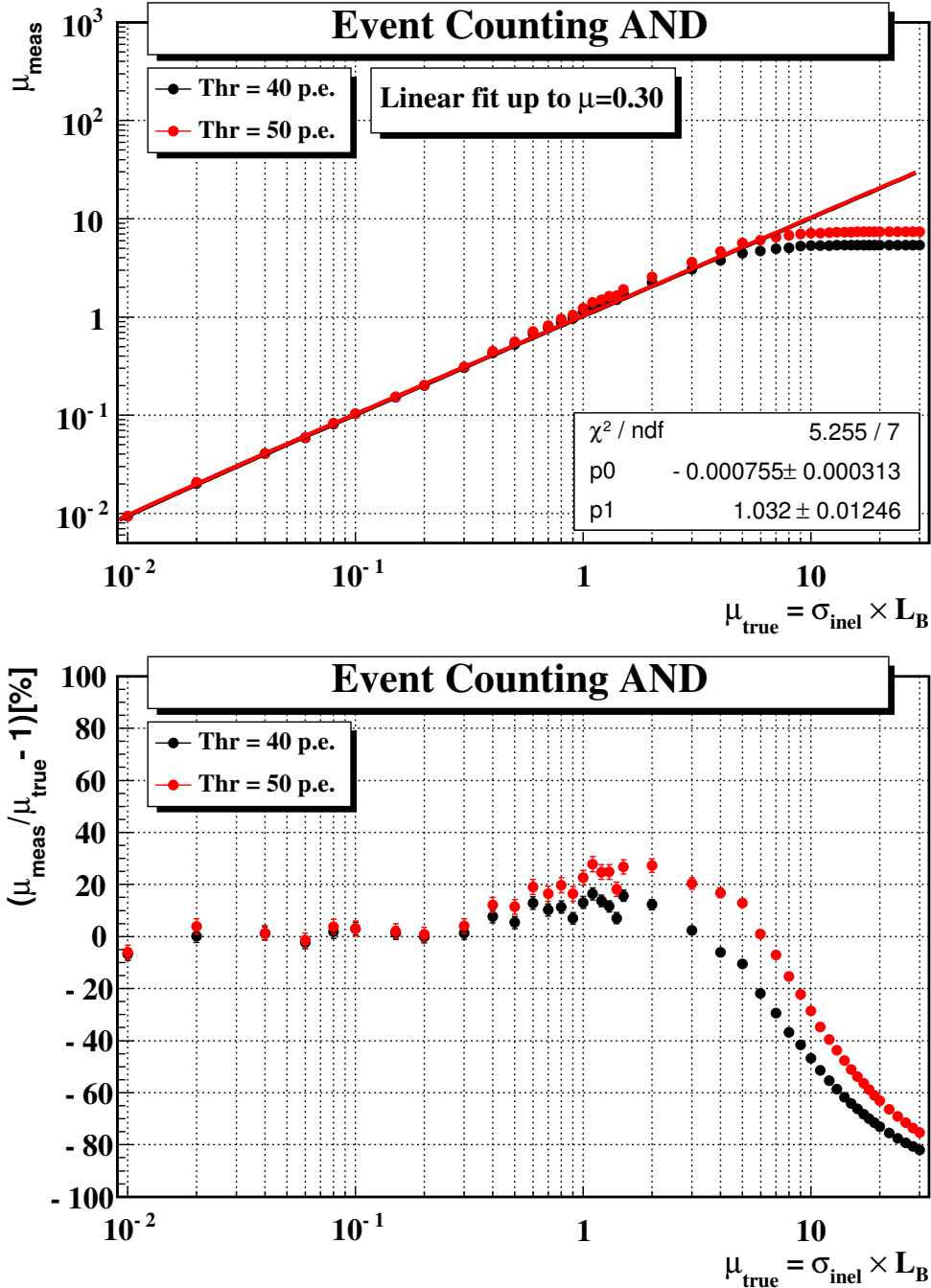
**Figure 35**. *Top: average number of pp interactions per event measured with a linear extrapolation of $P_{hits/BX}^{AND}$ from $\mu = 0.01$ for two different thresholds (40 and 50 p.e.). Bottom: deviation from the true value.*

## 5.5 Combinatorial model

### 5.5.3 Hit counting "OR"

With the hit counting "OR" method, the average number of $pp$ interactions per event is given by Equation 47 of Appendix D:

$$\mu = \frac{N^{OR}_{part/BX}}{N^{OR}_{part/pp}} = \frac{N_{pp}}{N_{BX}} \cdot \frac{\sum_{i=1}^{N_{BX}} \log\left(1 - \frac{N^{OR}_{hits}(i)}{N_{tubes}}\right)}{\sum_{j=1}^{N_{pp}} \log\left(1 - \frac{N^{OR}_{hits}(j)}{N_{tubes}}\right)} \tag{17}$$

The average number of particles per $pp$ interaction ($N^{OR}_{part/pp}$) is reported in Table 3. The measurements of $\mu$ as a function of the true values with the combinatorial model are plotted in Figure 36. The uncertainty on $N^{OR}_{part/pp}$ is neglected.

For $\mu < 1$, the difference between the measured and the true number of $pp$ interactions with two different thresholds (40 and 50 p.e.) is within the statistical uncertainty. For $\mu > 1$, $\mu$ is overestimated due to the migration effect (Section 5.3). By increasing the luminosity the migration effect gives an excess of particles compared to the prediction, therefore $\mu$ is overestimated. The deviation increases with the threshold due to an increased migration effect.

**Linear approximation**

For $\mu \ll 1$, $\mu$ is proportional to the average number of hits per event ($N^{OR}_{hits/BX}$):

$$\mu \xrightarrow{\mu \ll 1} \frac{N^{OR}_{hits/BX}}{N^{OR}_{hits/pp}} \tag{18}$$

The average number of hits per $pp$ interaction ($N^{OR}_{hits/pp}$) is reported in Table 3. The measurements of $\mu$ as a function of the true values with a linear extrapolation of $N^{OR}_{hits/BX}$ from $\mu = 0.01$ are plotted in Figure 37. A linear fit to the measured points up to $\mu_{true} = 1.0$ has a slope consistent with 1 and is consistent with going through the origin. This means that the measurement of $\mu$ with the linear approximation is reliable up to $\mu = 1.0$. For $\mu > 1$, $\mu$ is overestimated due to the migration effect. However, when $\mu$ becomes sufficiently large ($\mu > 5$), the **saturation effect** starts to play a role. The saturation effect in hit counting arises from counting hits instead of particles. The number of particles increases constantly with $\mu$ while the maximum number of hits is limited to 32 (the number of tubes). When $\mu$ is sufficiently large ($\mu > 5$), the large number of particles saturates the detector and lead to an underestimate of $\mu$. Since the migration effect leads to an overestimate and the saturation to an underestimate, these two effects cancel to some degree in the linear approximation.

Note that the logarithmic corrections do not improve the result of linear model in the range of validity $\mu < 1$.
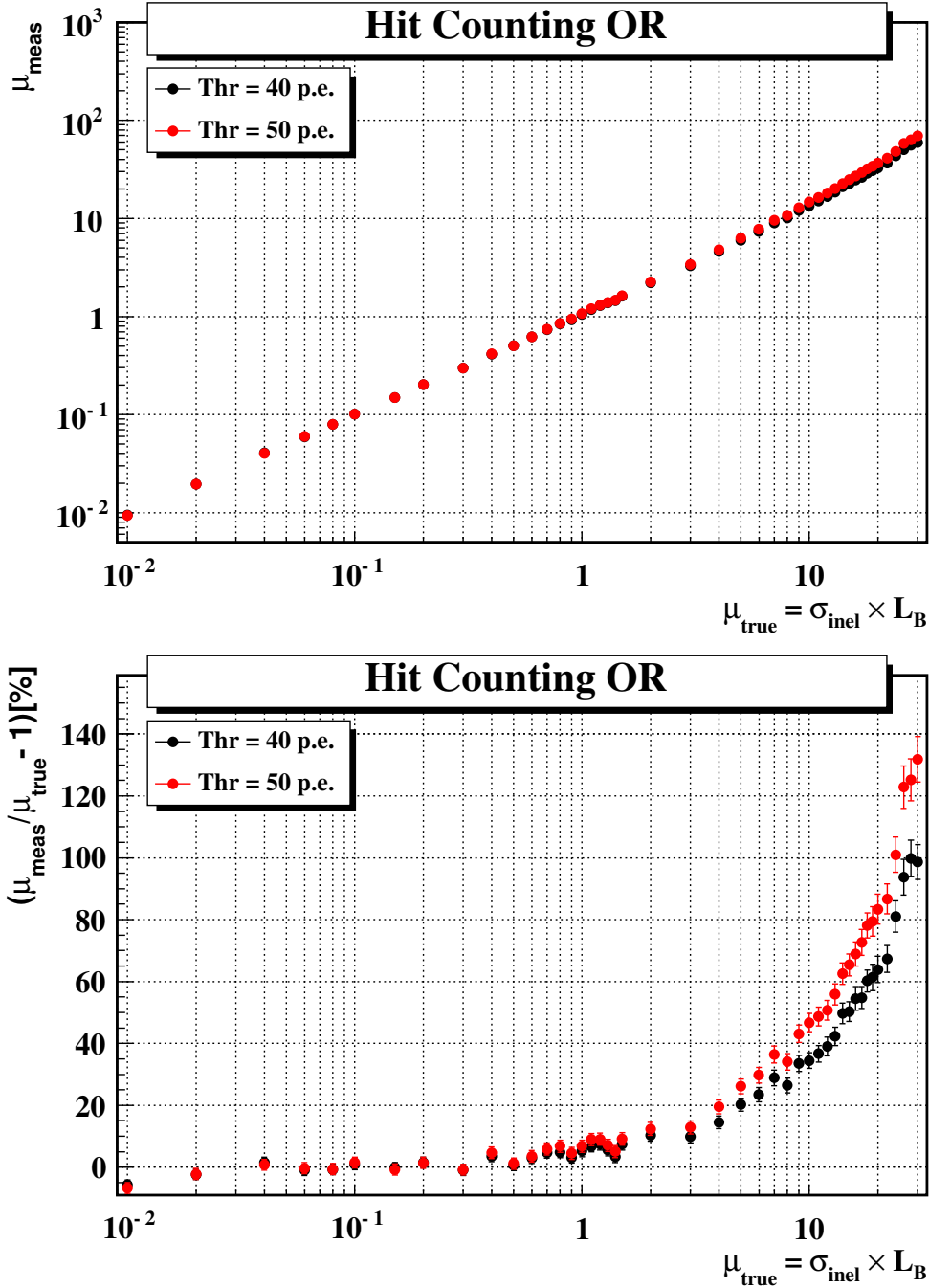
**Figure 36**. *Top: average number of pp interactions per event measured with the hit counting "OR" method as a function of the true value for two different thresholds (40 and 50 p.e.). Bottom: deviation from the true value.*
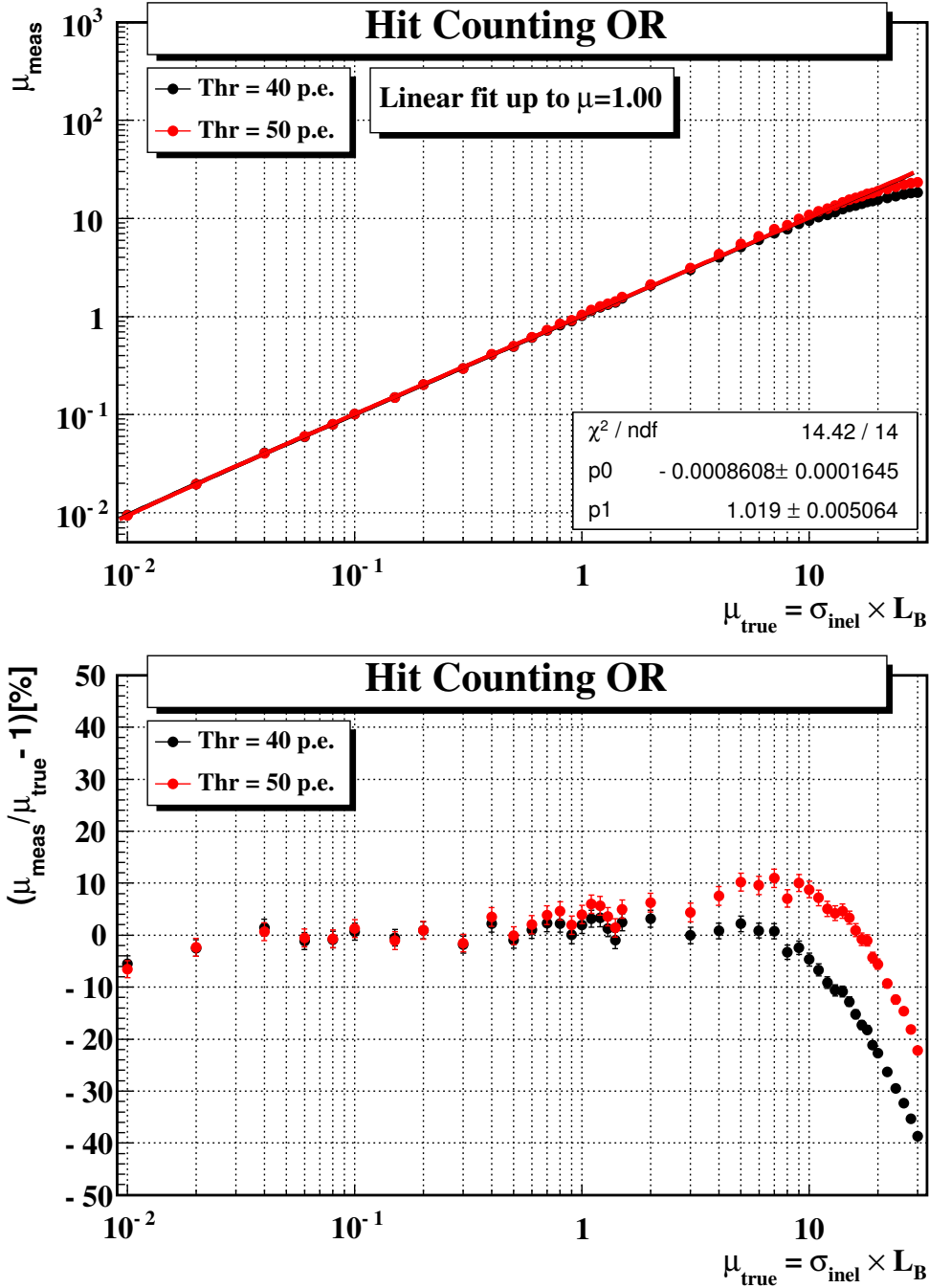
**Figure 37**. *Top: average number of pp interactions per event measured with a linear extrapolation of $N^{OR}_{hits/BX}$ from $\mu = 0.01$ for two different thresholds (40 and 50 p.e.). Bottom: deviation from the true value.*

## 5.5 Combinatorial model

### 5.5.4 Hit counting "AND"

The average number of $pp$ interactions per event is related to the average number of particle per event in coincidence mode by Equation 67 in Appendix E:

$$
\begin{aligned}
N^{AND}_{part/BX} = \quad & \mu N^{AND}_{part/pp} + \mu \left( N^{A}_{part/pp} - N^{AND}_{part/pp} \right) \left( 1 - e^{-\mu\varepsilon^{C}} \right) \\
& + \mu \left( N^{C}_{part/pp} - N^{AND}_{part/pp} \right) \left( 1 - e^{-\mu\varepsilon^{A}} \right)
\end{aligned}
\tag{19}
$$

where $N^{AND}_{part/BX}$ is evaluated with Equation 68 in Appendix E. The detection efficiencies ($\varepsilon^{A}$, $\varepsilon^{C}$ and $\varepsilon^{AND}$) and the average number of particles per $pp$ interaction ($N^{A}_{part/pp}$, $N^{C}_{part/pp}$ and $N^{AND}_{part/pp}$) can be found in Table 3. The average number of $pp$ interactions per event is obtained by numerical inversion of Equation 19 with a $10^{-10}$ precision:

$$
\mu = f^{-1}(N^{AND}_{part/BX})
\tag{20}
$$

The measurements of $\mu$ as a function of the true values with the combinatorial model are plotted in Figure 38. The uncertainty on $\mu$ is the maximum variation of $\mu$ corresponding to a $\pm 1\,\sigma$ variation of $N^{AND}_{part/BX}$. The uncertainty on the efficiencies is neglected. With two different thresholds (40 and 50 p.e.), the difference between the measured and the true number of $pp$ interactions is within the statistical uncertainty when $\mu < 1$. For $\mu > 1$, the number of detected particles is larger than the prediction due to the migration effect (Section 5.3) therefore $\mu$ is overestimated. The deviation increases with the threshold due to an increased migration effect.

**Linear approximation**

For $\mu \ll 1$, $\mu$ is proportional to the average number of hits per event ($N^{AND}_{hits/BX}$):

$$
\mu \xrightarrow{\mu \ll 1} \frac{N^{AND}_{part/BX}}{N^{AND}_{part/pp}} \xrightarrow{\mu \ll 1} \frac{N^{AND}_{hits/BX}}{N^{AND}_{hits/pp}}
\tag{21}
$$

The average number of hits per $pp$ interaction ($N^{AND}_{hits/pp}$) can be found in Table 3. The measurements of $\mu$ as a function of the true values with a linear extrapolation of $N^{AND}_{hits/BX}$ from $\mu = 0.01$ are plotted in Figure 39. A linear fit to the measured points up to $\mu_{true} = 0.1$ has a slope consistent with 1 and is consistent with going through the origin. This means that the measurement of $\mu$ with the linear approximation is reliable up to $\mu = 0.1$. For $\mu > 0.1$, $\mu$ is overestimated due to the effects of migration and coincidence. The total effect at $\mu = 1$ with a 50 $p.e.$ threshold is about 50%. For $\mu > 10$, saturation effect starts to play a role.

Note that the prediction of the combinatorial model with the hit counting "AND" method is as accurate as the hit counting "OR" method up to $\mu = 1$.
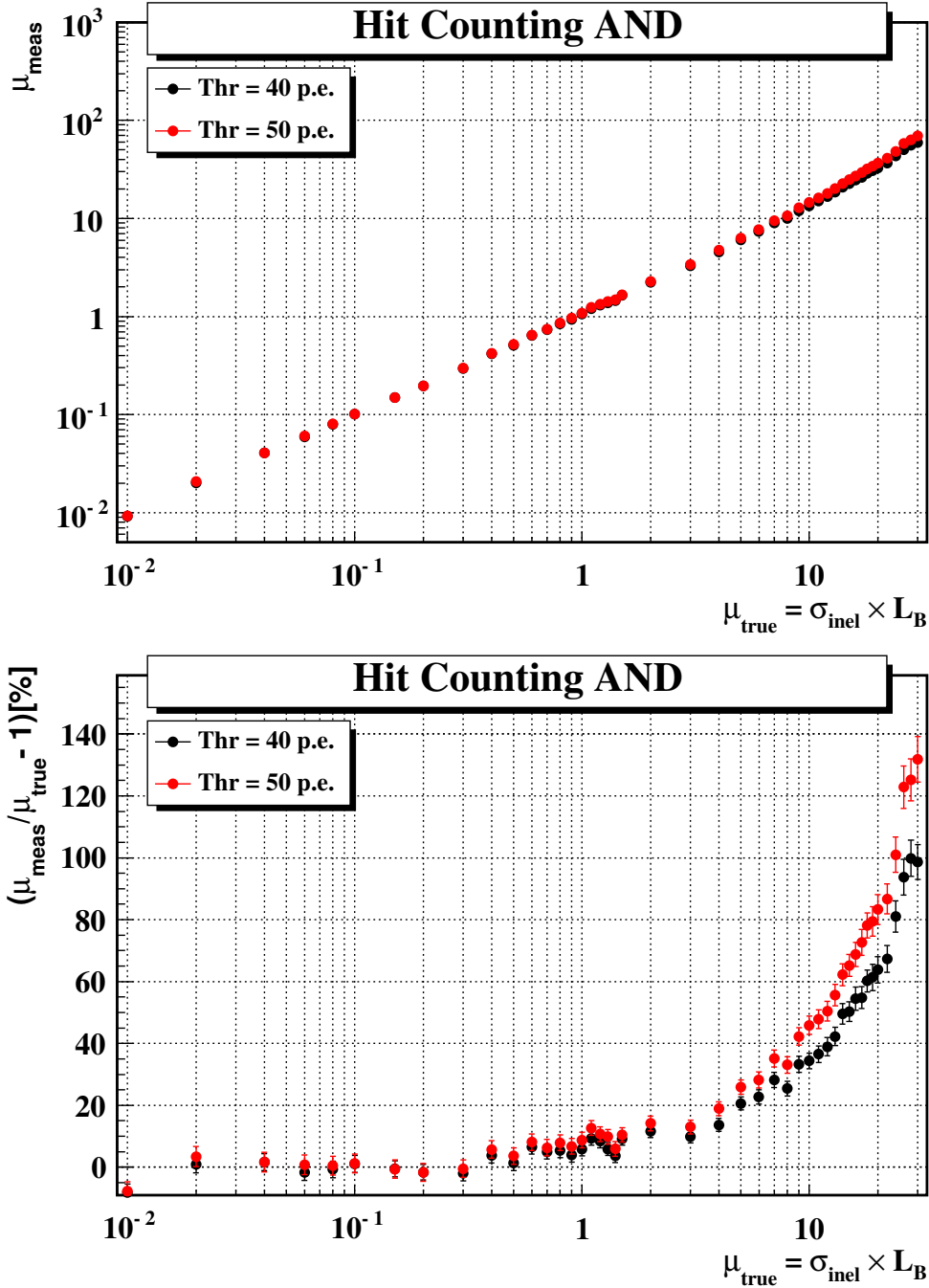
**Figure 38**. *Top: average number of pp interactions per event measured with the hit counting "AND" method as a function of the true value for two different thresholds (40 and 50 p.e.). Bottom: deviation from the true value.*
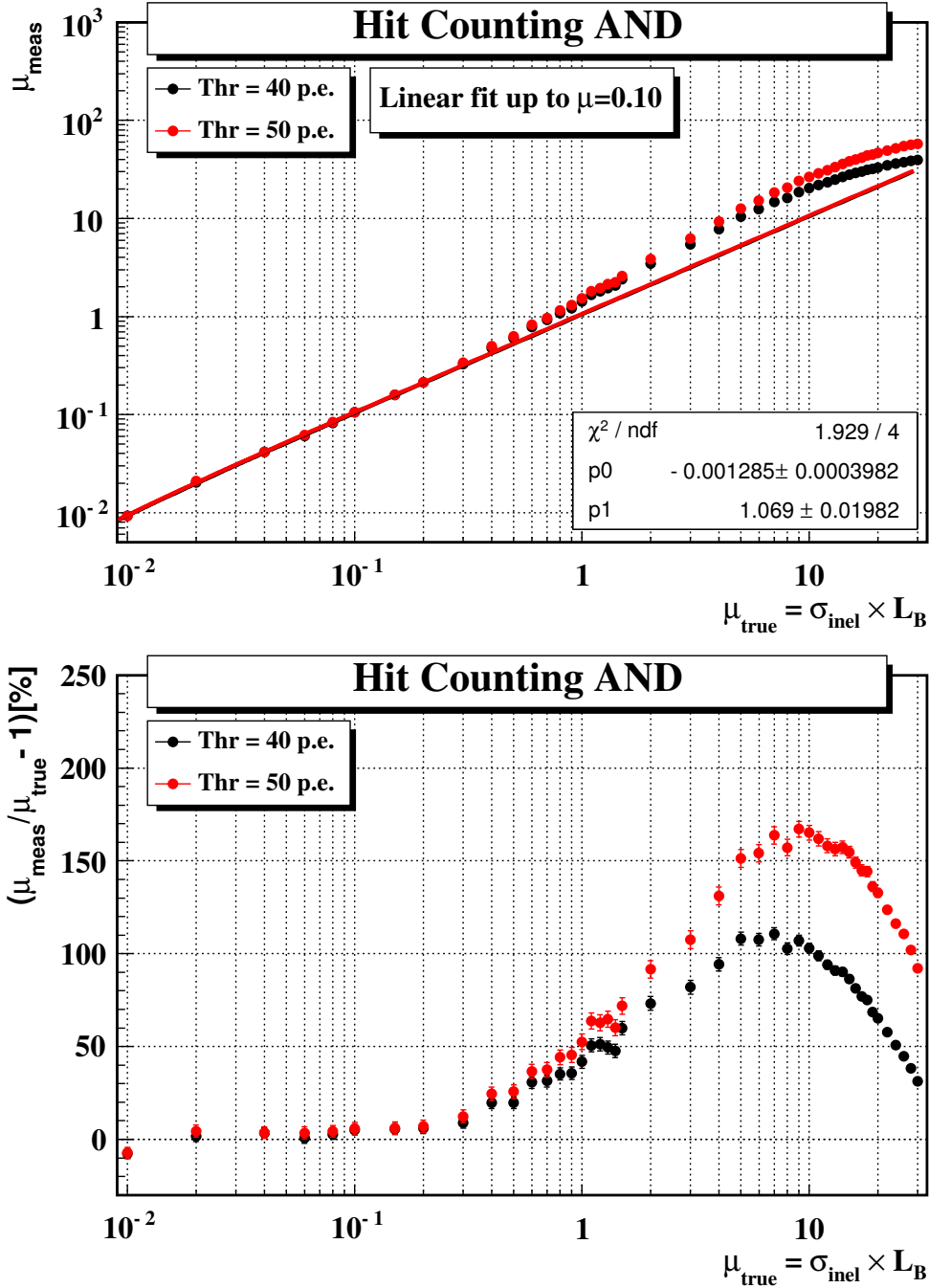
**Figure 39**. *Top: average number of pp interactions per event measured with a linear extrapolation of $N_{hits/BX}^{AND}$ from $\mu = 0.01$ for two different thresholds (40 and 50 p.e.). Bottom: deviation from the true value.*

## 5.6 Polynomial fit model

The average number of detected events ($P_{hits/BX}$) and the average number of hits per event ($N_{hits/BX}$) are not linear with $\mu$ for 3 reasons:

- Saturation effect;
- Combinatorial effect;
- Migration effect.

Saturation is due to the the limited number of available tubes in hit counting (32), while in event counting it is due to the lack of empty events at high luminosity. Combinatorial effects arise in coincidence mode, while the migration effect is due to the small signals at low $\mu$ which migrate above threshold at high $\mu$.

As discussed in the previous section, combinatorial and saturation effects have been analytically calculated. However, the migration effect produces a consistent overestimate of $\mu$ already at $\mu = 1$ for hit counting and has not been analytically evaluated. The accuracy of the luminosity monitor can be increased by parameterizing all non-linear effects with polynomial fits of $\mu$ as a function of $P_{hits/BX}$ for the event counting methods and $N_{hits/BX}$ for the hit counting methods. The degree of the polynomial fit depends on the counting method and on the range of $\mu$. To keep the order of the polynomial smaller than 4, the polynomial fit is performed in two different ranges of $\mu$.

To test the performance of the polynomial fit model, the Monte Carlo sample of 9159 single $pp$ interaction events is divided into two subsamples: one is used to perform the polynomial fit (**reference sample**), the other is used to test the luminosity monitoring performance (**measurement sample**). Both for reference and measurement samples, multiple $pp$ interaction events are created by randomly selecting single $pp$ interaction events and overlapping them according to a Poissonian distribution with average $\mu_{true}$ between 0.01 and 30.

### 5.6.1 Event counting

The average number of $pp$ interactions per event ($\mu$) as a function of the detected events rate ($P_{hits/BX}$) in the reference sample is fitted with a polynomial function

$$\mu = f(P_{hits/BX}) = \sum_{i=0}^{n} a_i P_{hits/BX}^i \tag{22}$$

The results of the fits for a 50 $p.e.$ threshold are shown in Figure 40 (event counting "OR") and Figure 41 (event counting "AND"). The polynomial fits are used to convert the average number of detected events observed in the measurement samples in the corresponding number of $pp$ interactions per event (Figure 42 and Figure 43). The slope of the linear fits is consistent with 1 which means that all non linear effects are taken into account up to $\mu = 8$.
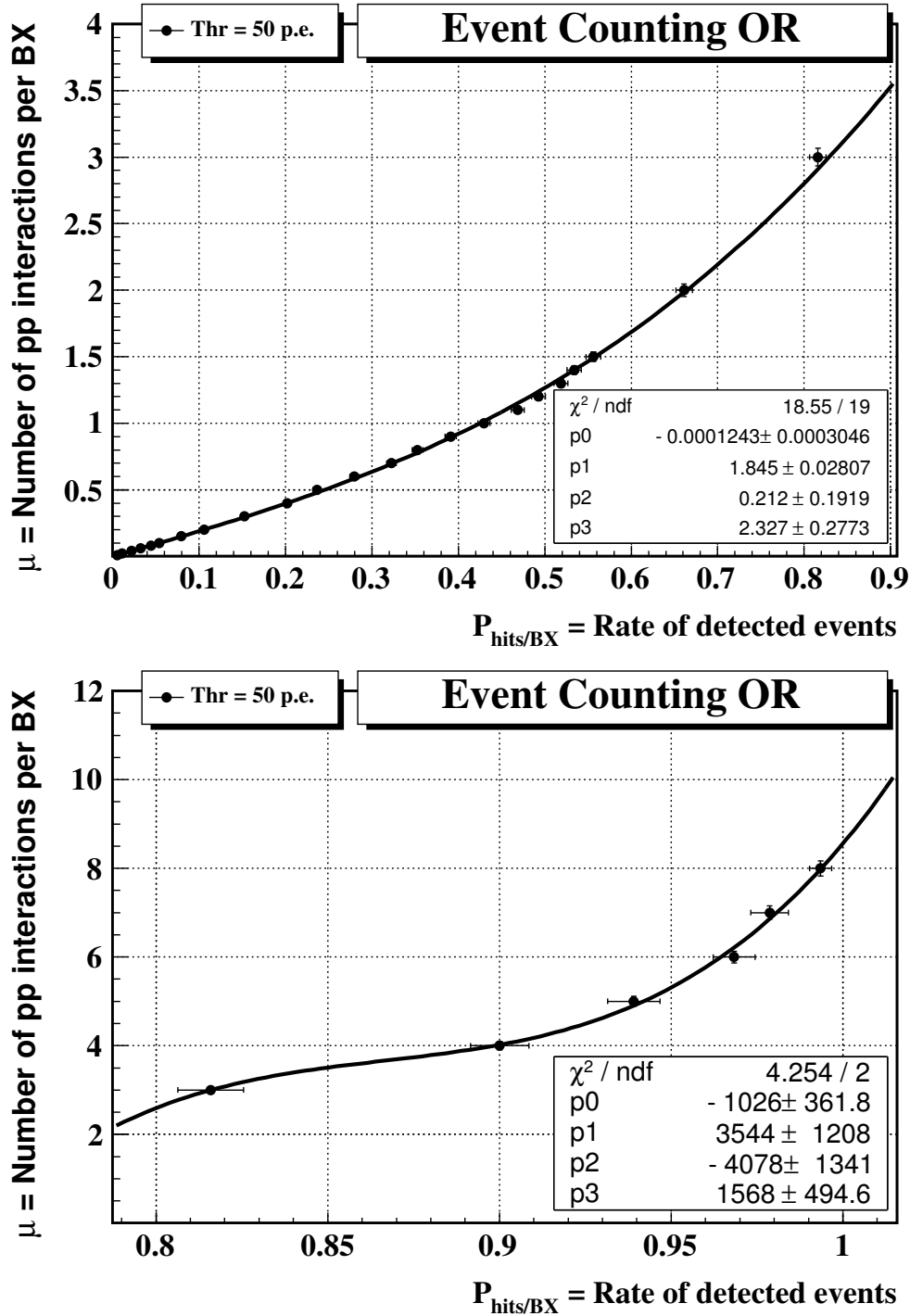
**Figure 40**. *Polynomial fits of the average number of pp interactions per event ($\mu$) as a function of the average number of detected events ($P_{hits/BX}$) with event counting "OR" method for $P_{hits/BX} < 0.8$ (top) for $P_{hits/BX} > 0.8$ (bottom).*

49
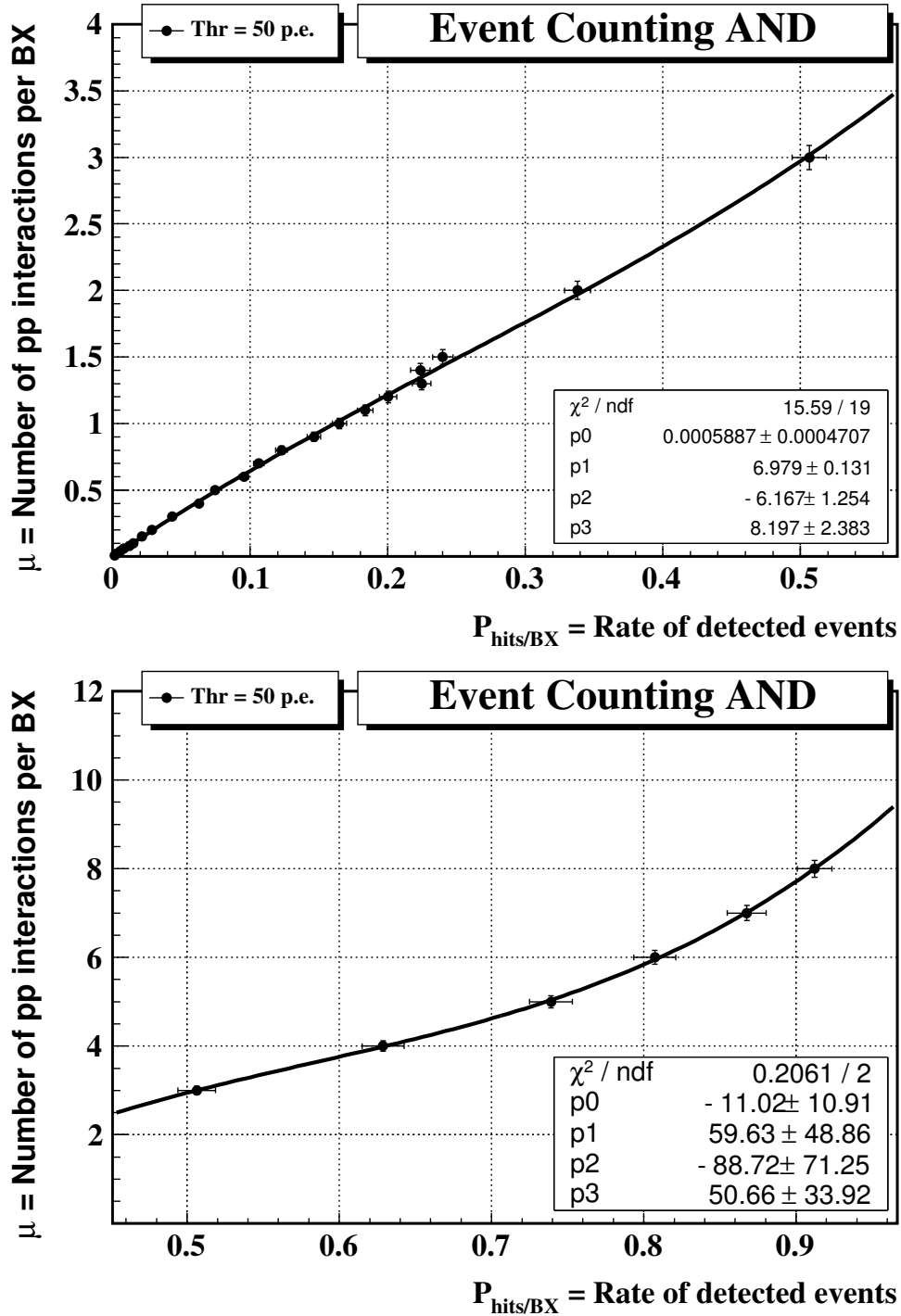
**Figure 41**. *Polynomial fits of the average number of pp interactions per event (μ) as a function of the average number of detected events ($P_{hits/BX}$) with event counting "AND" method for μ < 0.5 (top) for μ > 0.5 (bottom).*

50
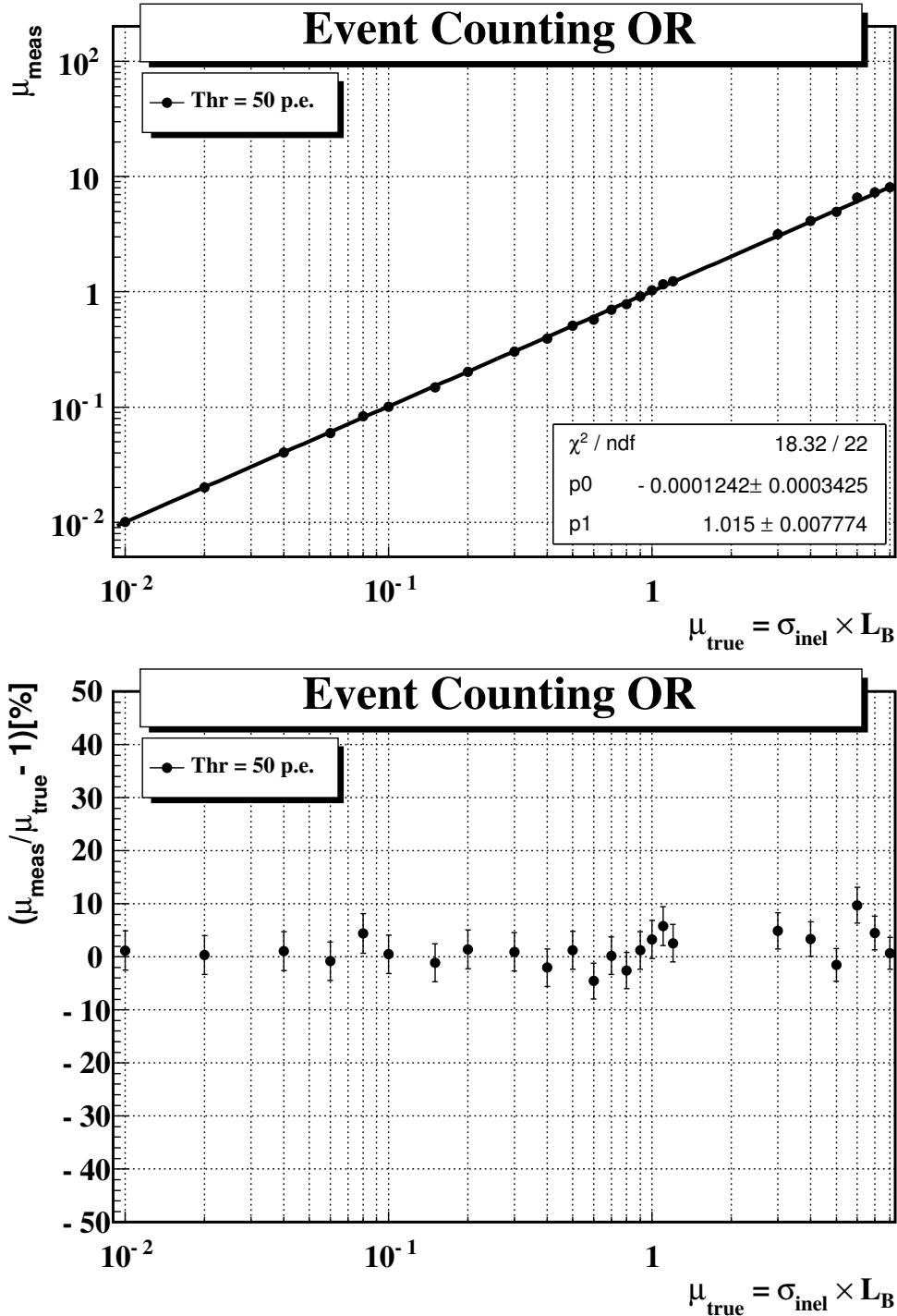
**Figure 42**. *Top: average number of pp interactions per event measured with the polynomial fit model by using the event counting "OR" method versus the true value. A linear fit is superimposed. Bottom: deviation from the true value.*
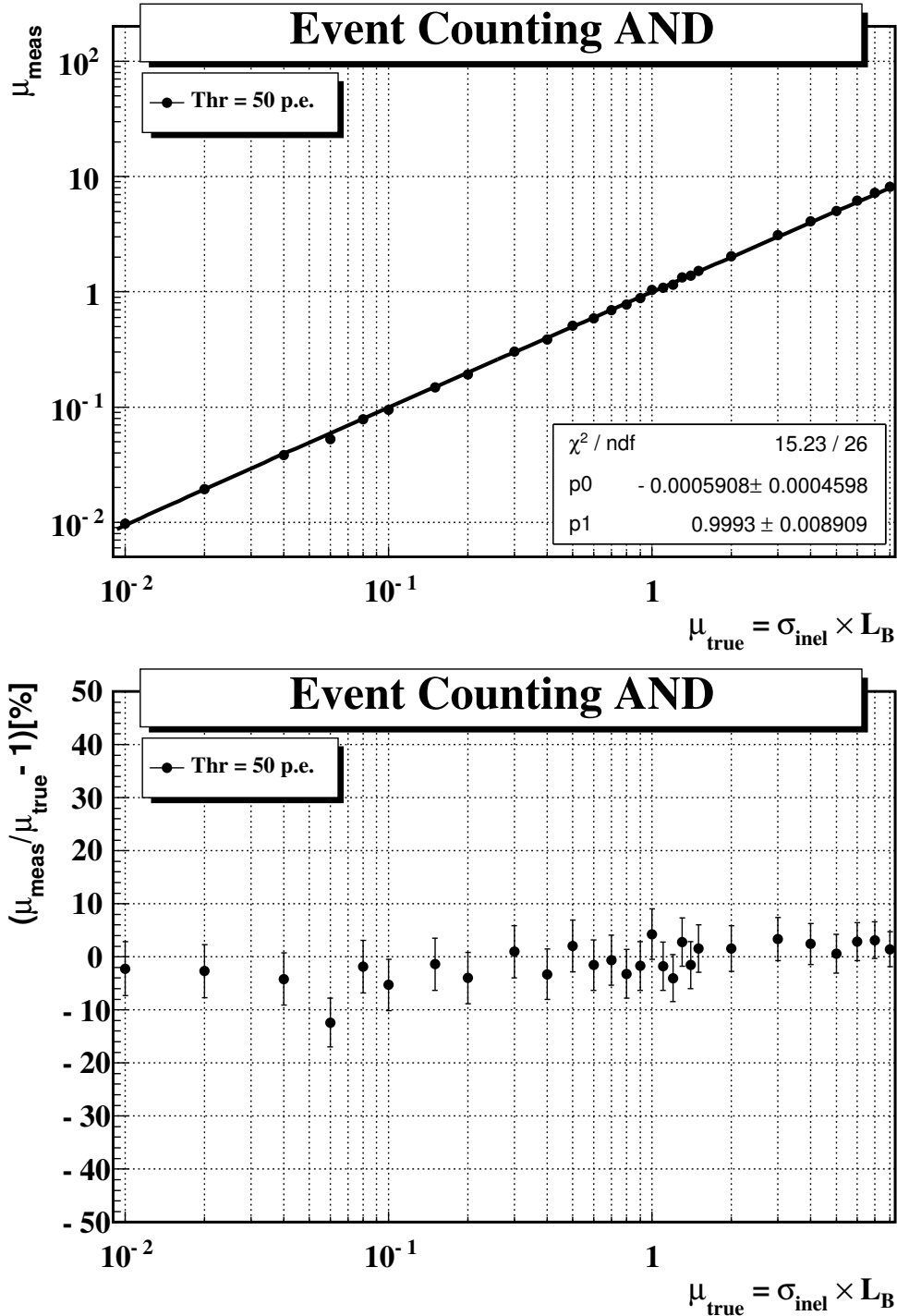
**Figure 43**. *Top: average number of pp interactions per event measured with the polynomial fit model by using the event counting "AND" method versus the true value. A linear fit is superimposed. Bottom: deviation from the true value.*

## 5.6    Polynomial fit model

### 5.6.2    Hit counting

The average number of $pp$ interactions per event ($\mu$) as a function of average number of hits per event ($N_{hits/BX}$) observed in the reference sample are fitted with a polynomial function

$$\mu = f(N_{hits/BX}) = \sum_{i=0}^{n} a_i N_{hits/BX}^i \qquad (23)$$

The results of the fits are shown for a 50 $p.e.$ threshold for both hit counting "OR" (Figure 44) and hit counting "AND" (Figure 45) methods.

The polynomial fits obtained from the reference samples are used to convert the average number of hits per event observed in the measurement samples in the corresponding number of $pp$ interactions per event (Figure 46 and Figure 47).

The slope of the linear fits are consistent with 1 which means that all non linear effects are taken into account in the luminosity range up to $\mu = 30$.
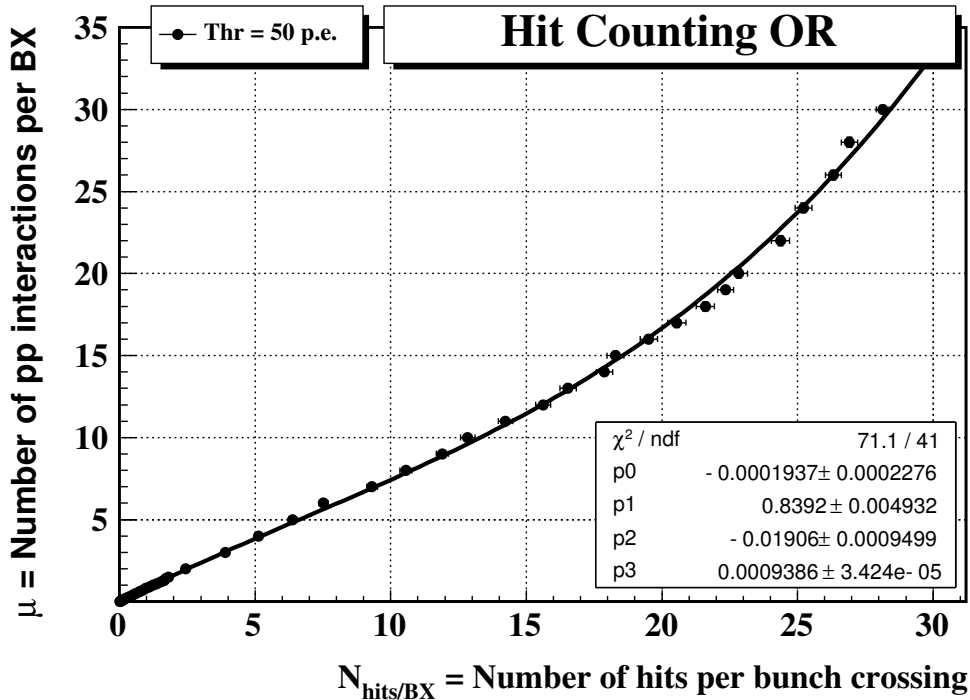


**Figure 44**. *Average number of pp interactions per event ($\mu$) as a function of the average number of hits per event ($N_{hits/BX}$) with the hit counting "OR" method. The distribution is fitted with a 4th degree polynomial in the whole range of $\mu$.*
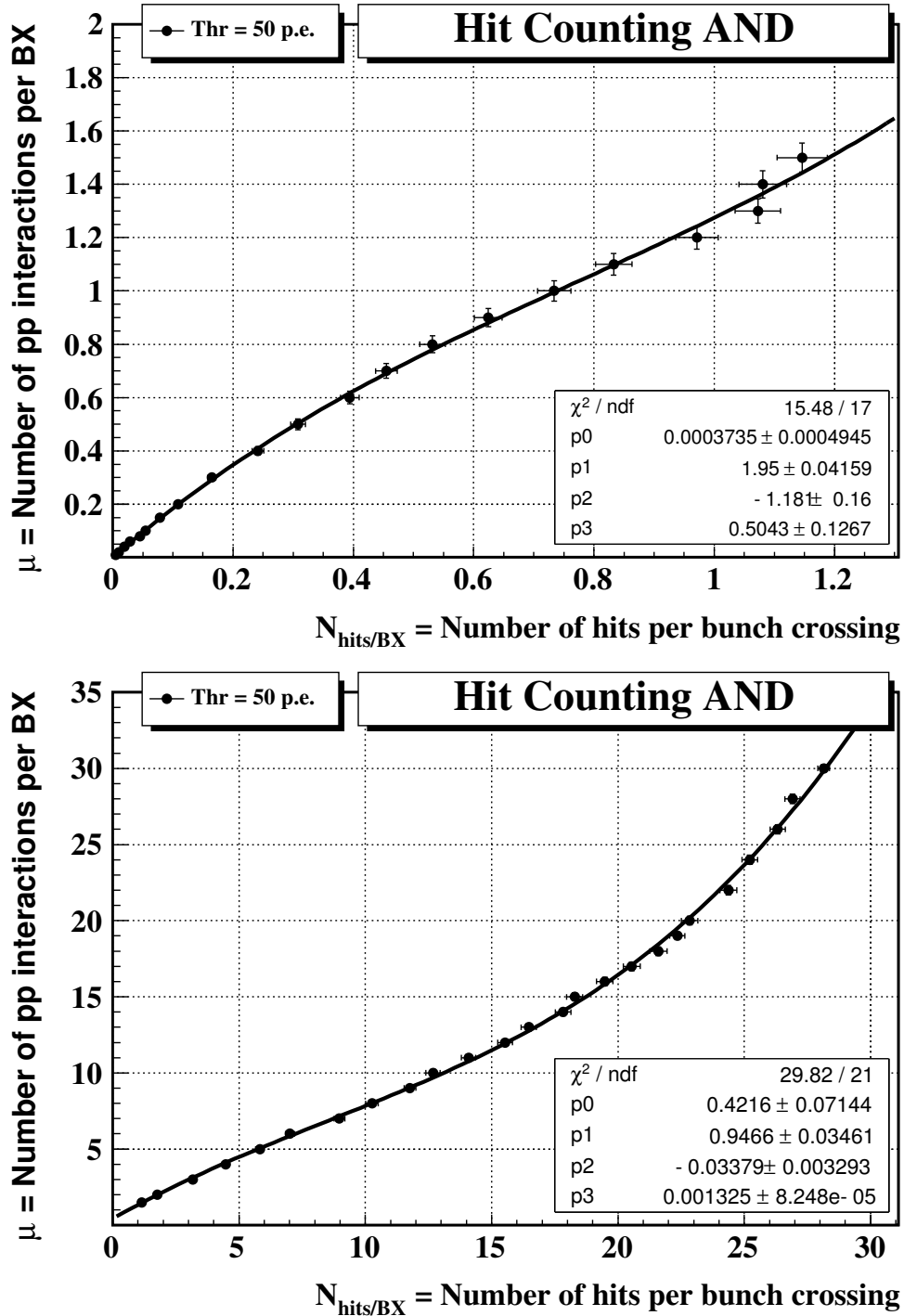
**Figure 45**. *Average number of pp interactions per event (μ) as a function of the average number of hits per event (N$_{hits/BX}$) with hit counting "AND" method. The distribution is fitted with a 4th degree polynomial for μ < 1.2 (top) and μ > 1.2 (bottom).*
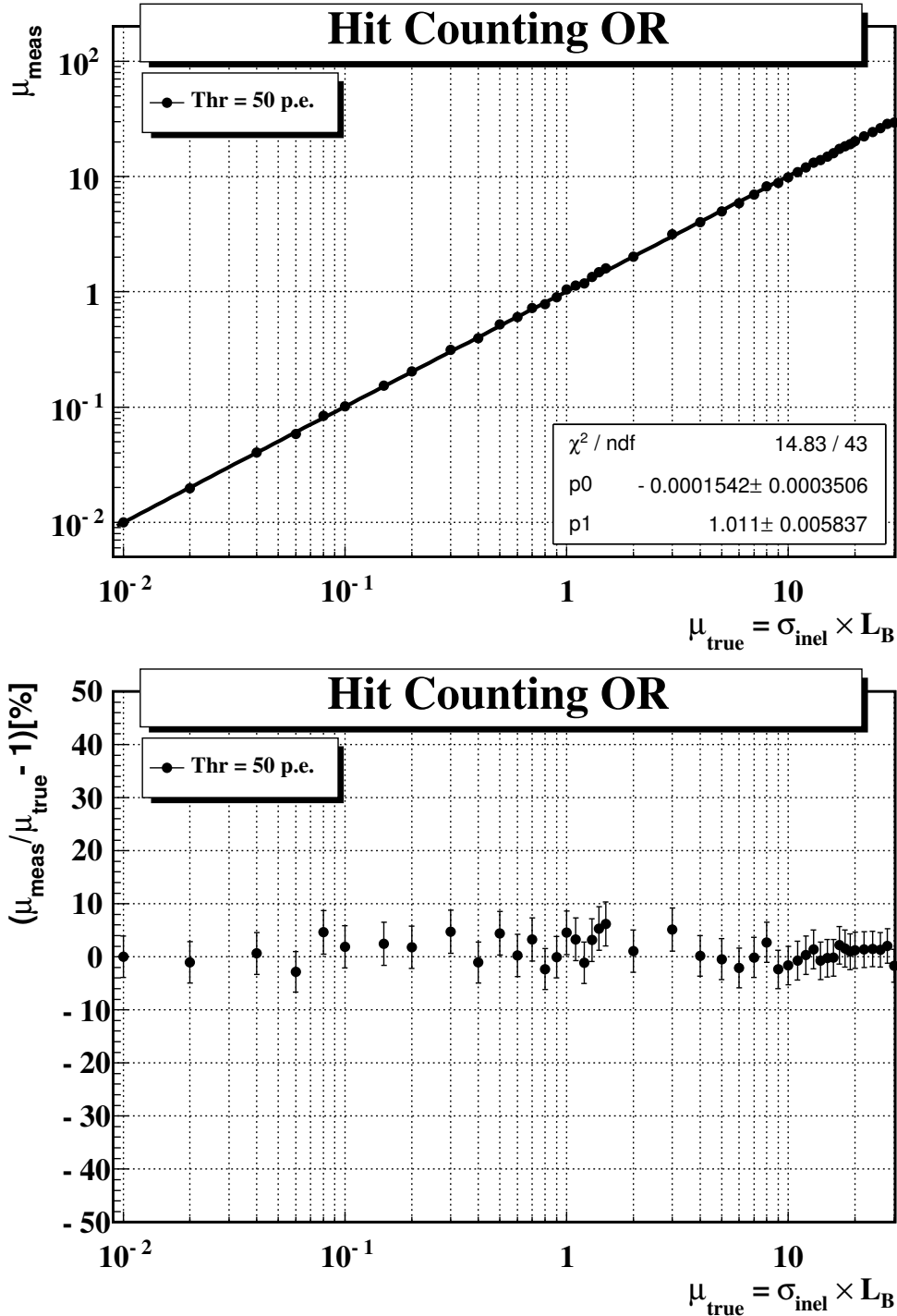
**Figure 46**. *Top: average number of pp interactions per event measured ($\mu_{meas}$) with the polynomial fit model with hit counting "OR" method versus the true value ($\mu_{true}$). A linear fit is superimposed. Bottom: deviation from the true value.*
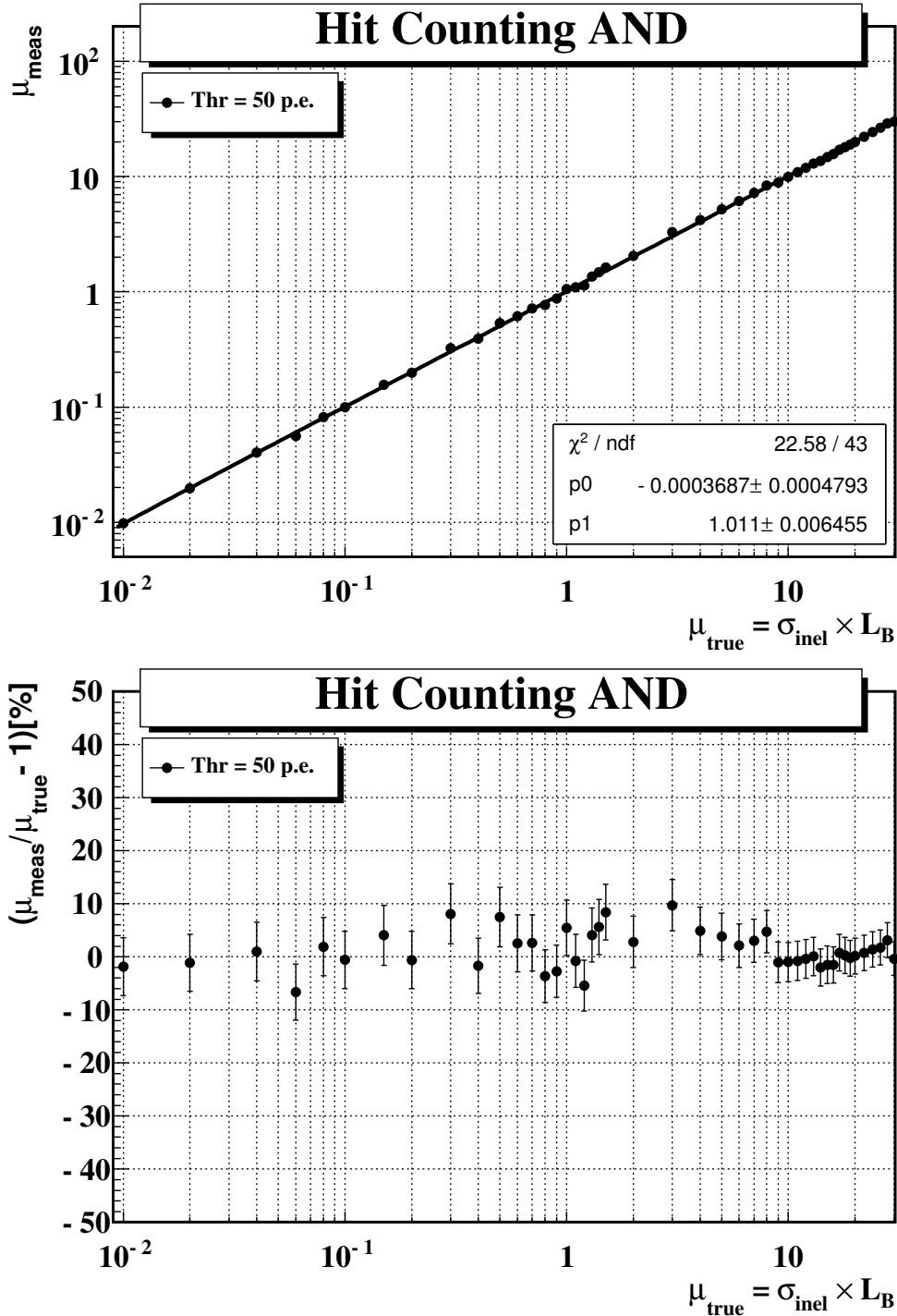
**Figure 47**. *Top: average number of pp interactions per event measured ($\mu_{meas}$) with the polynomial fit model with hit counting "AND" method versus the true value ($\mu_{true}$). A linear fit is superimposed. Bottom: deviation from the true value.*

# 6    Conclusions and summary

A stand-alone GEANT4 simulation of the LUCID detectors has been made. The response of the simulated detector to single particles has been studied for various particle types. Many parameters that influence the Cerenkov light collections has been implemented in the program. One of the results from this simulation was that pions traversing the Cerenkov tubes on-axis produce a clean Gaussian peak in the pulse-height distribution. The peak-value predicted for pions in the wavelength range [160 nm, 700 nm] was estimated to correspond to 103 *p.e.* (74 from the gas and 29 from the PMT window).

While pions traversing the Cerenkov tubes on-axis produce a Gaussian peak in the pulse-height distribution, this is not the case for pions interacting in the tube walls. Even if the wall is only one millimeter thick Aluminium, this material is enough to completely smear out the Gaussian peak observed in the on-axis distribution.

In ATLAS there is of course much more material that can produce secondary particles than the LUCID detector itself. LUCID detects charged particles in the pseudo-rapidity range [5.6, 6.2] and at these low angles the beampipe material that primary particles have to traverse before hitting LUCID is for example 15-20 cm thick.

A detailed Monte Carlo simulation of LUCID with all the detectors in ATLAS has been made with a two-step approach. The first step consisted of an event generation with the PHOJET program followed by a simulation of the interactions between primary particles and the detectors in ATLAS using the GEANT3-GCALOR program. The LUCID detector was simulated in the second step using the GEANT4 program, with the secondary particles created in the GEANT3-GCALOR simulation being an input to the LUCID simulation. The GEANT3-GCALOR program was used since it has been extensively studied and tested by the Radiation Task-force in ATLAS and it is believed that it gives one of the best available description of soft particle production.

The main complication of measuring luminosity at the LHC is the pile-up i.e. the fact that many interactions will occur in the same bunch crossing. In order to measure the luminosity it is therefore necessary to be able to determine the number of interaction per bunch crossing. This is not a trivial task and the main purpose of the present study was to study different algorithms that can be used to extract the number of interactions per bunch crossing.

Three classes of algorithms can be distinguished: Event counting methods, Hit counting methods and Particle counting methods. Particle counting without any requirement on a minimum number of particles is a perfectly "linear" method i.e. the number of interactions per bunch crossing is directly proportional to the number of particles going into the LUCID acceptance. This is not the case if one requires at least one particle in each of the two LUCID detectors. One can then use probability arguments to produce an expression that gives the number of particles in the LUCID

57

acceptance as a function of $\mu$. It is, however, not possible to analytically invert this expression so that $\mu$ is expressed as a function of the number of particles.

Particle counting is the easiest method to use but LUCID cannot be used to count particles in its present implementation and this method has therefore not been studied further in the present analysis. The other two methods (Hit counting and Event counting) suffer in addition to the combinatorial problem mentioned above also from saturation and so-called migration. These non-linear effects means that both Event and Hit counting are only proportional to $\mu$ for small $\mu$-values. Event counting can be done both in OR and in AND mode. In both cases a linear approximation works reasonably well up to a $\mu$ of 0.1. If a correction for the combinatorial effects is applied this range can be extended for both OR and AND mode to something like $\mu < 5$.

For the Hit counting method in OR mode, the somewhat surprising result was that a linear approximation gives a better result than a method that corrects for the combinatorial effects. The reason is that migration and saturation are two effects that to some extent cancel out and so if one correct for saturation but not migration, the results is worse than if no correction is made. With a linear approximation one can with an optimal choice of the threshold cut measure $\mu$ up to about 7-8. After a combinatorial correction, this value has decreased to something like 1.

For Hit counting in AND mode the conclusion is different. Here the combinatorial effects are much larger and a linear approximation breaks down already at a $\mu$ of 0.1. Corrections for the combinatorics increase in this case the $\mu$ range with an order of magnitude but this is of course still a low and not very useful $\mu$ range.

The overall conclusion at this stage is therefore that the best method to use is the Event counting AND method with a combinatorial correction. However, the useful $\mu$ range is then severely limited and the accuracy is in the order of 5%.

Much of the problems with the methods discussed above is that the migration effect cannot be described and corrected for in an analytical way. The approach adopted in the final part of this study is therefore to plot the number of interactions per bunch crossing as a function of the measured number of events or hits (without any corrections). This distribution is then fitted by a polynomial function and this fit function can then be used to estimate the luminosity. With this approach the luminosity can be measured correctly up to a $\mu$ value of around 10 with Event counting and 30 with Hit counting. These upper limits are caused by saturation since a detector with a limited number of channels cannot work when the $\mu$ value is so high that every channel gives a hit for every bunch crossing.

# A   Wavelength dependent parameters

| $\lambda$ [nm] | $C_4F_{10}$ Absorption Length [m] |
|:---:|:---:|
| 150 | 0.001 |
| 172 | 0.82 |
| 175 | 4 |
| 200 | 6 |
| 700 | 6 |

**Table 6**. *Absorption Length of $C_4F_{10}$ as a function of photon wavelength.*

| $\lambda$ [nm] | Aluminum Reflectivity | $\lambda$ [nm] | Aluminum Reflectivity |
|:---:|:---:|:---:|:---:|
| 150 | 0.022456 | 450 | 0.923245 |
| 175 | 0.227736 | 475 | 0.934399 |
| 200 | 0.388777 | 500 | 0.943149 |
| 225 | 0.515113 | 525 | 0.950013 |
| 250 | 0.614222 | 550 | 0.955398 |
| 275 | 0.691972 | 575 | 0.959622 |
| 300 | 0.752967 | 600 | 0.962936 |
| 325 | 0.800817 | 625 | 0.964399 |
| 350 | 0.838355 | 650 | 0.967576 |
| 375 | 0.867803 | 675 | 0.969176 |
| 400 | 0.890905 | 700 | 0.970431 |
| 425 | 0.909028 | | |

**Table 7**. *Aluminum Reflectivity as a function of photon wavelength.*

| $\lambda$ [nm] | $C_4F_{10}$ Quantum Efficiency | $\lambda$ [nm] | $C_4F_{10}$ Quantum Efficiency |
|---|---|---|---|
| 160 | 0.063096 | 440 | 0.246415 |
| 170 | 0.152522 | 450 | 0.237137 |
| 180 | 0.188365 | 460 | 0.232631 |
| 190 | 0.211349 | 470 | 0.219617 |
| 200 | 0.237137 | 480 | 0.207332 |
| 210 | 0.232631 | 490 | 0.195734 |
| 220 | 0.223872 | 500 | 0.177828 |
| 230 | 0.207332 | 510 | 0.161560 |
| 240 | 0.203392 | 520 | 0.146780 |
| 250 | 0.199526 | 530 | 0.133352 |
| 260 | 0.192014 | 540 | 0.125893 |
| 270 | 0.188365 | 550 | 0.114376 |
| 280 | 0.192014 | 560 | 0.101937 |
| 290 | 0.207332 | 570 | 0.077923 |
| 300 | 0.211349 | 580 | 0.055165 |
| 310 | 0.215443 | 590 | 0.044668 |
| 320 | 0.223872 | 600 | 0.036869 |
| 330 | 0.228209 | 610 | 0.029854 |
| 340 | 0.232631 | 620 | 0.021962 |
| 350 | 0.237137 | 630 | 0.017113 |
| 360 | 0.241732 | 640 | 0.012115 |
| 370 | 0.246415 | 650 | 0.008912 |
| 380 | 0.256055 | 660 | 0.005623 |
| 390 | 0.251189 | 670 | 0.003687 |
| 400 | 0.251189 | 680 | 0.002073 |
| 410 | 0.251189 | 690 | 0.001188 |
| 420 | 0.251189 | 700 | 0.000764 |
| 430 | 0.246415 | | |

**Table 8**. *Hamamatsu R762 PMT Quantum Efficiency as a function of photon wavelength.*

# B  Event Counting "OR"

The event rate in the "OR" counting mode ($P^{OR}_{hits/BX}$) can be written as

$$P^{OR}_{hits/BX} = 1 - P^{AND}_{0/BX} \tag{24}$$

where $P^{AND}_{0/BX}$ (rate of events with no hits in side A and C) is the sum of two terms:

  I -  probability of having 0 interactions;

  II -  probability of having $n$ interactions with 0 hits in both modules.

Assuming that interactions are Poissonian, Term I can be written as:

$$I = P_\mu(0) = \frac{e^{-\mu}\mu^0}{0!} = e^{-\mu} \tag{25}$$

Under the assumption that the probability to detect an interaction does not depend on the number of interactions in a given event, the combined probability of not detecting $n$ interactions in a event (Term II) can be written as:

$$II = (1 - \varepsilon^{OR})^n \tag{26}$$

where $\varepsilon^{OR}$ is the probability to detect an interaction in single side mode. This assumption is true only to a first approximation. In reality, being the hit detection dependent on an photoelectron threshold, if $n$ interactions are present in an event, the probability to see $n+1$ interactions is larger due to the migration effect (see Section 5.3). Term II is convoluted with a Poissonian distribution of average $\mu$ (the sum starts from $n = 1$ to avoid double counting of Term I):

$$\sum_{n=1}^{\infty}(1-\varepsilon^{OR})^n\frac{e^{-\mu}\mu^n}{n!} = \sum_{n=0}^{\infty}(1-\varepsilon^{OR})^n\frac{e^{-\mu}\mu^n}{n!} - e^{-\mu} = e^{-\varepsilon^{OR}\mu} - e^{-\mu} \tag{27}$$

The probability of observing an empty event is the sum of Equations 25 and 27:

$$P^{AND}_{0/BX} = e^{-\mu} + e^{-\varepsilon^{OR}\mu} - e^{-\mu} = e^{-\varepsilon^{OR}\mu} \tag{28}$$

Eventually, the event rate in the "OR" mode is

$$P^{OR}_{hits/BX} = 1 - P^{AND}_{0/BX} = 1 - e^{-\varepsilon^{OR}\mu} \tag{29}$$

This formula is obtained under the assumption that the probability of having $n$ interactions does not change in time. For this reason luminosity will be extracted separately for each filled bunch in a sufficiently small time period (*LumiBlock*).

# C   Event Counting "AND"

The event rate in the "AND" counting mode ($P_{hits/BX}^{AND}$) can be written as

$$P_{hits/BX}^{AND} = 1 - P_{0/BX}^{OR} \tag{30}$$

where $P_{0/BX}^{OR}$ (rate of events with no hits in side A or C) is the sum of four terms:

  I - probability of having 0 interactions;

 II - probability of having $n$ interactions with at least one detected in side A, together with any number not detected in both modules;

III - probability of having $n$ interactions with at least one detected in side C, together with any number not detected in both modules.

IV - probability of having $n$ interactions with 0 hits in both modules.

The calculation of all terms are performed under the same assumptions done in the previous section (efficiencies constant in time and no migration effect).

Assuming that interactions are Poissonian, Term I can be written as:

$$I = P_\mu(0) = \frac{e^{-\mu}\mu^0}{0!} = e^{-\mu} \tag{31}$$

To evaluate contributions II, III and IV, *exclusive* efficiencies to detect a interaction ($\varepsilon_1$, $\varepsilon_2$, $\varepsilon_3$ and $\varepsilon_0$) are defined in Table 9.

| | |
|---|---|
| $\varepsilon_1$ | probability of detecting an interaction in A, but not in C |
| $\varepsilon_2$ | probability of detecting an interaction in C, but not in A |
| $\varepsilon_3$ | probability of detecting an interaction in both modules |
| $\varepsilon_0$ | probability of detecting no interactions (=$1 - \varepsilon_1 - \varepsilon_2 - \varepsilon_3$) |

**Table 9**. *Exclusive detection efficiencies.*

*Exclusive* efficiencies in Table 9 are related to the *inclusive* efficiencies defined in Table 3 according to the formula:

$$\begin{aligned}
\varepsilon_1 &= \varepsilon^A - \varepsilon^{AND} \\
\varepsilon_2 &= \varepsilon^C - \varepsilon^{AND} \\
\varepsilon_3 &= \varepsilon^{AND} \\
\varepsilon_0 &= 1 - \varepsilon^A - \varepsilon^C + \varepsilon^{AND}
\end{aligned} \tag{32}$$

Term II (III) consists of all permutations of $k$ interactions detected in module A (C) and $n - k$ interactions not detected in any module:

$$II = \sum_{k=1}^{n} \varepsilon_1^k \, \varepsilon_0^{n-k} \binom{n}{k} = (\varepsilon_1 + \varepsilon_0)^n - \varepsilon_0^n \tag{33}$$

$$III = \sum_{k=1}^{n} \varepsilon_2^k \, \varepsilon_0^{n-k} \binom{n}{k} = (\varepsilon_2 + \varepsilon_0)^n - \varepsilon_0^n \tag{34}$$

Term IV is the probability of having an event with $n$ interactions which are not detected neither by any single module nor by the both modules together:

$$IV = \varepsilon_0^n \tag{35}$$

Terms II, III and IV are convoluted with a Poissonian distribution with a average $\mu$ (the sum starts from $n = 1$ to avoid double counting of Term I):

$$\sum_{n=1}^{\infty} \frac{e^{-\mu} \mu^n}{n!} [(\varepsilon_1 + \varepsilon_0)^n - \varepsilon_0^n] = e^{-\mu} \left[ e^{\mu(\varepsilon_1 + \varepsilon_0)} - e^{\mu \varepsilon_0} \right] \tag{36}$$

$$\sum_{n=1}^{\infty} \frac{e^{-\mu} \mu^n}{n!} [(\varepsilon_2 + \varepsilon_0)^n - \varepsilon_0^n] = e^{-\mu} \left[ e^{\mu(\varepsilon_2 + \varepsilon_0)} - e^{\mu \varepsilon_0} \right] \tag{37}$$

$$\sum_{n=1}^{\infty} \frac{e^{-\mu} \mu^n}{n!} \varepsilon_0^n = e^{-\mu} (e^{\mu \varepsilon_0} - 1) \tag{38}$$

The total probability of observing an empty event is the sum of Equations 31, 36, 37 and 38:

$$P_{0/BX}^{OR} = e^{-\mu(1 - \varepsilon_0 - \varepsilon_1)} + e^{-\mu(1 - \varepsilon_0 - \varepsilon_2)} - e^{-\mu(1 - \varepsilon_0)} \tag{39}$$

Given the relations in Table 9, Equation 39 can be written as:

$$P_{0/BX}^{OR} = e^{-\mu \varepsilon^A} + e^{-\mu \varepsilon^C} - e^{-\mu(\varepsilon^A + \varepsilon^C - \varepsilon^{AND})} \tag{40}$$

Eventually, the event rate in the "AND" mode is

$$P_{hits/BX}^{AND} = 1 - P_{0/BX}^{OR} = 1 - e^{-\mu \varepsilon^A} - e^{-\mu \varepsilon^C} + e^{-\mu(\varepsilon^A + \varepsilon^C - \varepsilon^{AND})} \tag{41}$$

63

# D   Hit Counting "OR"

Without requiring a coincidence between A and C detector modules, the average number of $pp$ collisions per event ($\mu$) is the ratio between the average number of particles per event ($N^{OR}_{part/BX}$) and those per $pp$ collision ($N^{OR}_{part/pp}$)

$$\mu = \frac{N^{OR}_{part/BX}}{N^{OR}_{part/pp}} \tag{42}$$

The LUCID detector does not count particles, it only count hits. The way particles are distributed among the tubes depends on the interaction type: non diffractive, single- and double-diffractive. Assuming that particles are spread uniformly over the detector (Figure 26 shows that this is true to a good extent) the number of detected particles per tube is $N_{part}/N_{tubes}$, where $N_{part}$ is the total number of detected particles and $N_{tubes} = 32$. Assuming that particles in a tube are distributed according to a Poissonian, the number of hits can be written as the product of the number of tubes times the probability to have at least one particle in a tube (namely a hit):

$$N_{hits} = N_{tubes} \left[ 1 - e^{-\frac{N_{part}}{N_{tubes}}} \right] \tag{43}$$

Equation 43 can be inverted to turn the number of hits into particles:

$$N_{part} = -N_{tubes} \log \left( 1 - \frac{N_{hits}}{N_{tubes}} \right) \tag{44}$$

Note that Equation 44 holds for one event. Since the logarithm goes to inifinity when $N_{hits} = 32$, $N_{part}$ is constrained to be at maximum 200. For $\mu < 30$, the probability to have more that 200 particles is negligible. For a sample of $N_{BX}$ events with an unknown $\mu$, one can write:

$$N^{OR}_{part/BX} = -\frac{N_{tubes}}{N_{BX}} \sum_{i=1}^{N_{BX}} \log \left( 1 - \frac{N_{hits}(i)}{N_{tubes}} \right) \tag{45}$$

where $N_{hits}(i)$ is the number of hits in the event $i$. Similarly, for a sample of $N_{pp}$ collision events, one can write:

$$N^{OR}_{part/pp} = -\frac{N_{tubes}}{N_{pp}} \sum_{j=1}^{N_{pp}} \log \left( 1 - \frac{N_{hits}(j)}{N_{tubes}} \right) \tag{46}$$

By using Equation 45 and Equation 46, Equation 42 becomes:

$$\mu = \frac{N_{pp}}{N_{BX}} \cdot \frac{\sum_{i=1}^{N_{BX}} \log \left( 1 - \frac{N_{hits}(i)}{N_{tubes}} \right)}{\sum_{j=1}^{N_{pp}} \log \left( 1 - \frac{N_{hits}(j)}{N_{tubes}} \right)} \tag{47}$$

# E Hit Counting "AND"

In coincidence mode, there are two possibilities to detect an event with multiple interactions. A *true* coincidence occurs when at least one interaction is detected simultaneously in both modules. A *fake* coincidence occurs when no interaction is detected simultaneously in both modules, but at least two interactions are separately detected in different modules.

In coincidence mode, the average number of detected particles in events with $n$ interactions is the sum of two contributions:

I - the event contains at least one interaction which is detected in both modules, together with any number of interactions which are only detected in module A and not in C, and vice versa;

II - the event contains 0 interactions detected in both modules, together with at least one interaction which is only detected in module A and one which is only detected in module C.

The average number of particles corresponding to Terms I and II is the sum of the probability of each configuration times the corresponding number of detected interactions, times the number of particles per detected interaction.

Four *exclusive* definitions of average number of particles in the whole detector per detected interaction are used (Table 11).

| | |
|---|---|
| $C_1$ | no. of particles per detected interaction in A, but not in C |
| $C_2$ | no. of particles per detected interaction in C, but not in A |
| $C_3$ | no. of particles per detected interaction in both modules |
| $C_4$ | no. of particles per detected interaction in any module, not in both |

**Table 10**. *Exclusive definitions of average number of particles.*

The probability of each configuration is evaluated by using the efficiencies to detect an interaction defined in Table 9 ($\varepsilon_1$, $\varepsilon_2$, $\varepsilon_3$ and $\varepsilon_0$), together with the efficiency to detect an interaction in any module, but not in both ($\varepsilon_4$).

Suppose $n$ interactions occurred in an event, Terms I and II can be written as:

$$I = \sum_{k=1}^{n} \varepsilon_3^k \binom{n}{k} \left[ \sum_{l=0}^{n-k} \varepsilon_4^l (1 - \varepsilon_4 - \varepsilon_3)^{n-k-l} \binom{n-k}{l} \right] [kC_3 + lC_4] \qquad (48)$$

$$II = \sum_{k=1}^{n} \varepsilon_1^k \binom{n}{k} \left[ \sum_{l=1}^{n-k} \varepsilon_2^l \varepsilon_0^{n-k-l} \binom{n-k}{l} \right] [kC_1 + lC_2] \qquad (49)$$

**Term I**   The first contribution consists of $k$ interactions detected in both modules, $l$ of the remaining $n-k$ interactions detected in only one module and the remaining $n-k-l$ interactions undetected.

The probability of detecting $k$ interactions in both modules is $\varepsilon_3^k$. The probability of detecting $l$ interactions in only one module is $\varepsilon_4^l$. The probability of not detecting $n-k-l$ interactions is $(1-\varepsilon_4-\varepsilon_3)^{n-k-l}$.

Binomial factors are used to account for all permutations of $k$ out of $n$ interactions and $l$ out of $n-k$ interactions.

The average number of particles given by $k$ interactions detected in both modules is $kC_3$, while that of $l$ interactions detected in one module is $lC_4$.

**Term II**   The second contribution consists of $k$ interactions detected in module A but not in C, $l$ of the remaining $n-k$ interactions detected in module C but not in A, and the remaining $n-k-l$ interactions undetected.

The probability of detecting $k$ interactions in module A is $\varepsilon_1^k$. The probability of detecting $l$ interactions in module C is $\varepsilon_2^l$. The probability of not detecting $n-k-l$ interactions is $\varepsilon_0^{n-k-l}$.

Binomial factors are used to account for all permutations of $k$ out of $n$ interactions and $l$ out of $n-k$ interactions.

The average number of particles given by $k$ interactions detected in both modules is $kC_1$, while that of $l$ interactions detected in one module is $lC_2$.

**Sum over $l$**   The $l$-sums in Equations 48 and 49 can be evaluated by means of the binomial theorem:

$$kC_3 \sum_{l=0}^{n-k} \varepsilon_4^l \, (1-\varepsilon_4-\varepsilon_3)^{n-k-l} \binom{n-k}{l} = kC_3(1-\varepsilon_3)^{n-k} \tag{50}$$

$$C_4 \sum_{l=0}^{n-k} l \, \varepsilon_4^l \, (1-\varepsilon_4-\varepsilon_3)^{n-k-l} \binom{n-k}{l} = C_4(n-k)\varepsilon_4(1-\varepsilon_3)^{n-k-1} \tag{51}$$

$$kC_1 \sum_{l=1}^{n-k} \varepsilon_2^l \varepsilon_0^{n-k-l} \binom{n-k}{l} = kC_1 \left[ (\varepsilon_0+\varepsilon_2)^{n-k} - \varepsilon_0^{n-k} \right] \tag{52}$$

$$C_2 \sum_{l=1}^{n-k} l\varepsilon_2^l \, \varepsilon_0^{n-k-l} \binom{n-k}{l} = C_2(n-k) \, \varepsilon_2(\varepsilon_0+\varepsilon_2)^{n-k-1} \tag{53}$$

**Sum over $k$**   Equations 50-53 are used to evaluate the $k$-sums in Equations 48 and 49 by means of the binomial theorem:

$$C_3 \sum_{k=1}^{n} k\varepsilon_3^k (1-\varepsilon_3)^{n-k} \binom{n}{k} = C_3 \varepsilon_3 n \tag{54}$$

$$C_4 \varepsilon_4 \sum_{k=1}^{n} n\varepsilon_3^k (1-\varepsilon_3)^{n-k-1} \binom{n}{k} = C_4 \varepsilon_4 n \left[ \left( \frac{1}{1-\varepsilon_3} \right) - (1-\varepsilon_3)^{n-1} \right] \tag{55}$$

$$-C_4 \varepsilon_4 \sum_{k=1}^{n} k\varepsilon_3^k (1-\varepsilon_3)^{n-k-1} \binom{n}{k} = -C_4 \varepsilon_4 n \frac{\varepsilon_3}{1-\varepsilon_3} \tag{56}$$

$$C_1 \sum_{k=1}^{n} k\varepsilon_1^k (\varepsilon_0 + \varepsilon_2)^{n-k} \binom{n}{k} = C_1 \varepsilon_1 n (\varepsilon_0 + \varepsilon_1 + \varepsilon_2)^{n-1} \tag{57}$$

$$-C_1 \sum_{k=1}^{n} k\varepsilon_1^k \varepsilon_0^{n-k} \binom{n}{k} = -C_1 \varepsilon_1 n (\varepsilon_0 + \varepsilon_1)^{n-1} \tag{58}$$

$$C_2 \varepsilon_2 \sum_{k=1}^{n} n\varepsilon_1^k (\varepsilon_0 + \varepsilon_2)^{n-k-1} \binom{n}{k} = C_2 \varepsilon_2 n \left[ \frac{(1-\varepsilon_3)^n}{\varepsilon_0 + \varepsilon_2} - (\varepsilon_0 + \varepsilon_2)^{n-1} \right] \tag{59}$$

$$-C_2 \varepsilon_2 \sum_{k=1}^{n} k\varepsilon_1^k (\varepsilon_0 + \varepsilon_2)^{n-k-1} \binom{n}{k} = -C_2 \varepsilon_2 n \varepsilon_1 \frac{(1-\varepsilon_3)^{n-1}}{\varepsilon_0 + \varepsilon_2} \tag{60}$$

**Sum of Terms I and II**   Given that $C_1 \varepsilon_1$ is the number of particles registered in the whole detector when the interaction is detected in module A only and $C_2 \varepsilon_2$ is the number of particles registered in the whole detector when the interaction is detected in module C only, the sum of these Terms gives the number of particles registered in the whole detector when the interaction is detected in module A or in module C but not in both ($C_4 \varepsilon_4$):

$$C_4 \varepsilon_4 = C_1 \varepsilon_1 + C_2 \varepsilon_2 \tag{61}$$

Using Equation 61, the sum of Equations 54-60 gives:

$$I + II = C_3 \varepsilon_3 n + C_1 \varepsilon_1 n \left[ 1 - (\varepsilon_0 + \varepsilon_1)^{n-1} \right] + C_2 \varepsilon_2 n \left[ 1 - (\varepsilon_0 + \varepsilon_2)^{n-1} \right] \tag{62}$$

**Poissonian sum** The average number of particles per event in coincidence mode is given by the convolution of Equation 62 with a Poissonian of average $\mu$:

$$N^{AND}_{part/BX} = \sum_{n=0}^{\infty} (I + II) \frac{e^{-\mu}\mu^n}{n!} \tag{63}$$

Given the relations:

$$\sum_{n=0}^{\infty} n \frac{e^{-\mu}\mu^n}{n!} = \mu \qquad \text{and} \qquad \sum_{n=0}^{\infty} \frac{k^n}{n!} = e^k \tag{64}$$

Equation 63 becomes:

$$N^{AND}_{part/BX} = C_3\varepsilon_3\mu + C_1\varepsilon_1\mu \left[1 - e^{-\mu(\varepsilon_2+\varepsilon_3)}\right] + C_2\varepsilon_2\mu \left[1 - e^{-\mu(\varepsilon_1+\varepsilon_3)}\right] \tag{65}$$

The *inclusive* average numbers of particles are defined in Table 11.

| | |
|---|---|
| $N^A_{part/pp^*}$ | no. of particles per interaction detected in A (regardless of C) |
| $N^C_{part/pp^*}$ | no. of particles per interaction detected in C (regardless of A) |
| $N^{AND}_{part/pp^*}$ | no. of particles per interaction detected in both modules |

**Table 11**. *Inclusive definitions of average number of particles.*

Using relation 32 and the following ones:

$$\begin{aligned}
C_1\varepsilon_1 &= N^A_{part/pp^*}\varepsilon^A - N^{AND}_{part/pp^*}\varepsilon^{AND} = N^A_{part/pp} - N^{AND}_{part/pp} \\
C_2\varepsilon_2 &= N^C_{part/pp^*}\varepsilon^C - N^{AND}_{part/pp^*}\varepsilon^{AND} = N^C_{part/pp} - N^{AND}_{part/pp}
\end{aligned} \tag{66}$$

Equation 65 can be written as:

$$\begin{aligned}
N^{AND}_{part/BX} = \ &\mu N^{AND}_{part/pp} + \mu \left(N^A_{part/pp} - N^{AND}_{part/pp}\right)\left(1 - e^{-\mu\varepsilon^C}\right) \\
&+ \mu \left(N^C_{part/pp} - N^{AND}_{part/pp}\right)\left(1 - e^{-\mu\varepsilon^A}\right)
\end{aligned} \tag{67}$$

The average number of particles per event can be extracted from the number of hits per event as it was done for the single side mode (Equation 44 in Appendix D):

$$N^{AND}_{part/BX} = -\frac{N_{tubes}}{N_{BX}} \sum_{i=1}^{N_{BX}} \log\left(1 - \frac{N_{hits}(i)}{N_{tubes}}\right) \tag{68}$$

# References

[1] S. Agostinelli *et al.*, NIM **A506** (2003) 250.

[2] Hamamatsu private communication.

[3] J. D. Jackson, *Classical Electrodynamics*, Wiley & Sons, 1975.

[4] R. Arnold *et al.*, NIM **A270** (1988) 289.

[5] http://en.wikipedia.org.

[6] http://geant4.cern.ch/G4UsersDocuments/UsersGuides/PhysicsReferenceManual.

[7] W. R. Leo, *Techniques for Nuclear and Particle Physics Experiments*, Springer, 1987.

[8] R. Engel, *Phojet manual*, http://www-ik.fzk.de/ engel/phojet.html.

[9] http://www.staff.uni mainz.de/zeitnitz/Gcalor/gcalor.html.

[10] G. A. Schuler and T. Sjostrand, Phys. Rev. **D49** (1994) 2257.

[11] T. Sjostrand *et al.*, hep-ph/0603175.

[12] W. Bell, ATL-PHYS-PROC-2009-051; ATL-COM-PHYS-2009-156.

[13] G. Aad *et al.*, arXiv:0901.0512v4.

[14] S. Baranov *et al.*, ATL-GEN-2005-001.